

# At the stellar noise frontier: a transit survey of 121 TESS M3–M6 dwarfs

Yohann Tschudi<sup>1</sup> 

Independent Researcher, 69480 Anse, France  
e-mail: yohann.tschudi@gmail.com

Submitted to Astronomy & Astrophysics (manuscript ref. aa59754-26)

## ABSTRACT

**Context.** M-dwarf stars are the most favorable hosts for detecting small transiting planets, yet mid-to-late M-dwarfs that acquired sufficient TESS multi-sector coverage only through recent Cycle 6+ observations represent a newly accessible discovery space.

**Aims.** This paper presents a systematic transit survey of 121 M3–M6 dwarfs ( $T_{\text{eff}} = 2700\text{--}3400\text{ K}$ ) selected as “newly enabled” targets—stars with  $\leq 2$  archival TESS sectors that only recently crossed the multi-sector detection threshold, covering  $P = 0.5\text{--}100\text{ d}$ .

**Methods.** The sample was selected from 498 312 TIC M-dwarfs via a 9-step funnel. The pipeline combines TLS with a signal validation cascade, TRICERATOPS vetting, Gaia DR3 verification, and three empirical signal reliability tests.

**Results.** Pipeline validation achieved 100% recovery (16/16 planets) on 10 known systems with zero false positives. The survey identifies **20 transit-like signals** across 16 systems, none with prior TOI designations. The reliability framework classifies 2 as Tier 1 (High Robustness), 7 as Tier 2 (Moderate), and 10 as Tier 3 (Noise-Susceptible); one monotransit is excluded. No candidate SDE significantly exceeds its host star’s noise floor. The global false alarm rate is 17.4% (21/121; Wilson 95% CI: [11.6%, 25.1%]).

**Conclusions.** The survey quantifies TLS sensitivity limits on active M3–M6 dwarfs with sparse TESS coverage. The 2 Tier 1 candidates are priorities for RV confirmation. The 10 Tier 3 candidates require additional TESS sectors to establish signal persistence; 9 systems need high-resolution imaging.

**Key words.** planets and satellites: detection – planets and satellites: terrestrial planets – techniques: photometric – stars: low-mass

## 1. Introduction

M-dwarf stars, comprising approximately 70% of all stars in the solar neighborhood (Henry et al. 2006), are the most favorable hosts for detecting small transiting planets. Their small radii ( $0.1\text{--}0.6 R_{\odot}$ ) produce deeper transit signals for a given planet size, and their proximity to the Sun enables detailed follow-up with current and upcoming facilities (Kempton et al. 2018). The Kepler mission established that small planets ( $R_p < 1.5 R_{\oplus}$ ) are abundant around M-dwarfs, with an occurrence rate of  $\sim 2.5$  planets per star for  $P < 200\text{ d}$  (Dressing & Charbonneau 2015). Yet the census of sub-Earths ( $R_p < 1.0 R_{\oplus}$ ) from TESS remains sparse: most TESS surveys of M-dwarfs are restricted to short periods ( $P < 7\text{ d}$ ; Ment & Charbonneau 2023) or bright targets ( $T_{\text{mag}} < 10.5$ ; Guerrero et al. 2021).

The Transiting Exoplanet Survey Satellite (TESS; Ricker et al. 2015) has systematically observed the entire sky, with the ecliptic poles receiving continuous coverage spanning multiple years. This accumulated baseline fundamentally transforms the detection space for transiting planets: while single 27-day sectors limit searches to periods  $P \lesssim 13$  days, baselines exceeding 1000 days enable detection of planets with periods up to  $P \sim 70\text{--}100$  days ( $P_{\text{max}} = 0.7B$ ), probing a parameter space inaccessible to single-sector surveys.

With TESS Cycle 6+ observations (Sectors 80+, 2024–2025), a new population of M3–M6 dwarfs has crossed the multi-sector detection threshold: stars that had  $\leq 2$  archival sectors and only recently acquired sufficient coverage for transit searches at extended periods. Previous large-scale surveys focused on bright stars amenable to radial velocity follow-up

(Guerrero et al. 2021) or employed reliability-optimized thresholds that prioritize high-confidence candidates at the expense of completeness in the small-planet regime (Thompson et al. 2018). This newly available coverage is exploited to conduct a deliberate test of TLS detection limits on active mid-to-late M-dwarfs—probing the stellar noise frontier identified in this survey’s title.

This paper presents a systematic transit survey of 121 M-dwarf stars spanning spectral types M3–M6 ( $T_{\text{eff}} \approx 2700\text{--}3400\text{ K}$ ), specifically selected as “newly enabled” targets: stars that only became searchable through the accumulation of recent TESS sectors, with confirmed single-star status from Gaia DR3 astrometry. The survey covers the full accessible period range ( $P = 0.5\text{--}100\text{ d}$ ). The sample includes 2 M6 dwarfs (deepest transits,  $\sim 4000\text{ ppm}$  for Earth-sized planets), 22 M4–M5 dwarfs (moderate depths, extended periods accessible with typical baselines), and 97 M3 dwarfs (shallowest transits, longest accessible periods).

A pipeline was developed and validated based on Transit Least Squares (TLS; Hippke & Heller 2019) with Scout/Sniper optimization for computational efficiency on long baselines, enabling systematic exploration of the period-radius parameter space with false-positive rejection through multi-stage vetting with TRICERATOPS (Tool for Rating Interesting Candidate Exoplanets and Reliability Analysis of Transits Originating from Proximate Stars; Giacalone et al. 2021). While TLS provides a detection threshold ( $SDE \geq 7$ ), the false alarm rate on active M-dwarfs with sparse multi-sector coverage remains poorly characterized empirically. This work addresses this gap by combining detection with a systematic signal reliability assessment

based on three independent empirical tests (circular shift FAR, lightcurve inversion, Fourier phase scrambling).

The approach presented here differs from existing TESS pipelines in several key aspects (Table 1):

While each individual component has precedents (TLS, TRICERATOPS, GP detrending), the combination targets a specific niche: (1) **extended period search** ( $P_{\max} = 0.7B$ , reaching 50–100 d) via multi-sector stitching, extending searchable periods from  $P \lesssim 7$  d (single sector) to  $P \sim 50$ –100 d; (2) **18-check signal validation cascade** targeting M-dwarf-specific false positives (BY Dra variability, harmonic nests); and (3) **Gaia DR3 physical verification** systematically integrated into the pipeline for direct background eclipsing binary exclusion.

The remainder of this paper is organized as follows: target selection (Sect. 2), detection and validation methodology including the signal reliability framework (Sect. 3), injection-recovery completeness tests (Sect. 4), pipeline robustness on known systems (Sect. 5), limitations (Sect. 6), results including signal reliability assessment (Sect. 7), discussion (Sect. 8), and conclusions (Sect. 9).

## 2. Target Selection Strategy

### 2.1. The “Newly Enabled M3–M6” Sample: 9-Step Selection Funnel

The central challenge in designing this survey was identifying M-dwarfs where transit detection at extended periods has *only recently become possible*—stars overlooked by existing surveys due to insufficient temporal coverage. For M3–M6 dwarfs, multi-sector baselines of several hundred to  $>2500$  d extend the searchable period range to  $P \sim 50$ –100 d, well beyond the reach of single-sector surveys.

To isolate the target population, a 9-step selection funnel was applied to the 498 312 TIC M-dwarfs, progressively narrowing to stars that crossed the multi-sector detectability threshold with TESS Cycle 6+ observations:

#### 2.1.1. Sample Composition by Spectral Type

The sample is restricted to spectral types M3–M6 ( $T_{\text{eff}} = 2700$ –3400 K), excluding earlier M-dwarfs (M0–M2) for two reasons:

**(1) Transit depth:** For M0–M2 dwarfs ( $T_{\text{eff}} > 3400$  K,  $R_{\star} \approx 0.4$ – $0.6 R_{\odot}$ ), Earth-sized transits produce  $\delta \approx 300$ –600 ppm, approaching the detection threshold (Signal Detection Efficiency,  $\text{SDE} \geq 7$ ; Hippke & Heller 2019) and increasing false positive rates.

**(2) Multi-sector coverage:** The “newly enabled” selection, by construction, has limited archival data. For M0–M2 dwarfs, transit depths for Earth-sized planets fall below the detection threshold and multi-sector coverage is insufficient for extended-period searches in this sample.

Table 3 summarizes the sample composition. The M3–M6 range provides complementary detection sensitivities:

**M6 dwarfs** ( $R_{\star} \approx 0.15 R_{\odot}$ ,  $T_{\text{eff}} = 2700$ –2900 K): Deepest transits ( $\delta \approx 3700$  ppm for  $1 R_{\oplus}$ ), enabling sub-Earth detection even with sparse coverage, but rare in magnitude-limited samples ( $N = 2$ ).

**M4–M5 dwarfs** ( $R_{\star} \approx 0.20$ – $0.25 R_{\odot}$ ,  $T_{\text{eff}} = 2900$ –3200 K): The “sweet spot” combining moderate transit depths ( $\delta \approx 1300$ –2100 ppm for  $1 R_{\oplus}$ ) with extended-period sensitivity well-matched to the survey baselines ( $N = 22$ ).

**M3 dwarfs** ( $R_{\star} \approx 0.30$ – $0.35 R_{\odot}$ ,  $T_{\text{eff}} = 3200$ –3400 K): Shallower transits ( $\delta \approx 700$ –950 ppm for  $1 R_{\oplus}$ ) requiring higher

SNR and longer baselines, but representing the largest subsample ( $N = 97$ ).

### 2.2. Selection Criteria

Each step in Table 2 is motivated by specific scientific or technical requirements. The rationale for each criterion is detailed below:

**Step 1–2: Spectral type restriction** ( $T_{\text{eff}} = 2700$ –3400 K). The lower bound ( $T_{\text{eff}} \geq 2700$  K) excludes late M-dwarfs with poorly constrained stellar parameters. The upper bound ( $T_{\text{eff}} \leq 3400$  K) excludes M0–M2 dwarfs where transit depths for Earth-sized planets fall below the detection threshold and multi-sector coverage is insufficient for extended-period searches (see Sect. 2.1.1).

**Step 3: Stellar radius** ( $R_{\star} < 0.35 R_{\odot}$ ). This ensures transit depths  $\delta > 800$  ppm for Earth-sized planets, well above the detection limit. Larger radii produce shallower transits that approach the noise floor.

**Step 4: Magnitude range** ( $T_{\text{mag}} = 8.0$ –12.5). The lower limit excludes ultra-bright stars with severe instrumental red noise ( $\beta > 5$ ), which prevents reliable transit detection even for known planets (see Sect. 6). The upper limit ensures sufficient photometric precision ( $\sigma < 1000$  ppm/hr) for Earth-sized transit detection.

**Step 5: Contamination ratio** ( $< 0.05$ ). Nearby sources contributing  $>5\%$  flux dilute transit depths and introduce false positive scenarios. This threshold ensures that even 1000 ppm transits remain detectable after dilution correction.

**Step 6: Minimum sectors** ( $\geq 3$ ). Multiple sectors provide: (1) period disambiguation through phase coherence, (2) SNR boost from transit stacking, and (3) harmonic rejection via transit count verification.

**Step 7: “Newly enabled” criterion** ( $\leq 2$  archival sectors,  $\geq 1$  Cycle 6 sector, baseline  $B > 100$  d). This is the central innovation of this survey. The strategy targets stars that were *not* previously searchable at extended periods (insufficient archival coverage) but *became* searchable with recent TESS observations (Cycle 6+, Sectors 80+). Planets at periods  $P = 10$ –100 d require multi-sector coverage to accumulate  $\geq 3$  transits for reliable period determination. With 3 sectors spread across TESS cycles,  $B$  can reach 700–2600 days despite only  $\sim 80$  days of actual photometry (Table B.1). This criterion isolates genuinely unexplored discovery space, avoiding targets already examined by archival mining surveys.

**Step 8: Gaia Renormalised Unit Weight Error (RUWE)** ( $< 1.4$ ). The standard threshold from Lindegren et al. (2021) is adopted to exclude unresolved binaries. Elevated RUWE indicates excess astrometric scatter from unresolved companions, which dilute transit depths and complicate interpretation.

**Step 9: No known planets/TESS Objects of Interest (TOIs)**. Targets with existing TOI alerts or confirmed planets are excluded to focus on previously unsearched systems.

The final sample comprises 121 M-dwarf stars representing a well-defined, previously unexplored parameter space for transit detection around mid-to-late M-dwarfs. With the sample defined, the following section describes the methodology employed to search these targets for transiting planets.

## 3. Methodology

Detecting small planets around faint M-dwarfs requires careful attention to both signal extraction and false-positive rejec-

**Table 1.** Comparison of transit detection pipelines.

Aspect	SPOC/QLP	SHERLOCK <sup>a</sup>	Nigraha <sup>b</sup>	This work
Algorithm	BLS	TLS/BLS	TLS + ML	TLS
Detrending	PDC	Savitzky-Golay	Standard	GP + Wotan
Multi-sector	Per-sector	Yes	Per-sector	Stitched (3–10)
Validation	TOI alerts	Statistical	Neural net	TRICERATOPS
Specificity	All stars	General	Shallow transits	M3–M6 noise frontier

**Notes.** BLS = Box Least Squares; TLS = Transit Least Squares; ML = Machine Learning; PDC = Pre-search Data Conditioning; GP = Gaussian Process; SPOC = Science Processing Operations Center; QLP = Quick Look Pipeline. TRICERATOPS is defined in Sect. 3.4.1. <sup>a</sup>Dévora-Pajares et al. (2024). <sup>b</sup>Rao et al. (2021).

**Table 2.** Newly Enabled M3–M6 selection funnel. Counts based on TIC v8.2 cross-matched with TESS observation logs through Sector 97 and Gaia DR3.

Step	Criterion	Targets	Justification
1	TIC M-dwarfs ( $T_{\text{eff}} \leq 4000$ K)	498 312	Complete M-dwarf base
2	$T_{\text{eff}} = 2700\text{--}3400$ K (M3–M6)	114 107	Deep transits ( $>800$ ppm for $1 R_{\oplus}$ )
3	$R_{\star} < 0.35 R_{\odot}$	59 414	Depth $>1000$ ppm for $1 R_{\oplus}$
4	$T_{\text{mag}} = 8.0\text{--}12.5$	1 852	Avoids saturation and faint noise
5	Contamination ratio $< 0.05$	1 475	Dilution $<5\%$
6	$\geq 3$ total sectors	1 061	Period disambiguation + SNR
7	Newly enabled <sup>a</sup> : $\leq 2$ archival + $\geq 1$ Cycle 6 + $B > 100$ d	199	<b>Not searchable before Cycle 6</b>
8	Gaia RUWE $< 1.4$	174	Excludes unresolved binaries
9	No TOI / known planet	<b>121</b>	Pure discovery targets

**Notes.** All counts are exact, derived from TIC v8.2 (steps 1–5) and `lightkurve` sector-level cross-match through Sector 97 (steps 6–7). RUWE = Renormalised Unit Weight Error. TOI = TESS Object of Interest. <sup>a</sup>The three sub-criteria are logically linked:  $\leq 2$  archival sectors combined with  $\geq 3$  total guarantees  $\geq 1$  recent sector and  $B > 100$  d.

**Table 3.** Sample distribution by spectral type.

Type	$T_{\text{eff}}$ (K)	N
M6	2700–2900	2
M4–M5	2900–3200	22
M3	3200–3400	97
<b>Total</b>	2700–3400	<b>121</b>

tion. The pipeline processes TESS photometry through six sequential stages, each addressing specific challenges: (1) data acquisition via quality cascade (SPOC  $\rightarrow$  TESS-SPOC  $\rightarrow$  QLP) to maximize photometric precision, (2) Gaussian Process (GP)-based preprocessing and sector stitching to remove stellar variability while preserving transit shapes, (3) TLS transit detection with  $SDE \geq 7$  threshold to identify candidate signals, (3b) harmonic nest cleanup via cross-masking and system parsimony for multi-candidate systems, (4) TRICERATOPS statistical vetting to quantify false-positive probabilities, and (5) Gaia DR3 physical verification to directly test background eclipsing binary scenarios.

### 3.1. Data Acquisition and Preprocessing

TESS photometry was retrieved using `lightkurve` (Lightkurve Collaboration 2018) with a quality cascade prioritizing SPOC (2-min) over TESS-SPOC over QLP (30-min). Each sector is normalized by median flux with asymmetric sigma-clipping ( $4\sigma$  above,  $20\sigma$  below to preserve deep transits).

Stellar parameters ( $R_{\star}$ ,  $M_{\star}$ ,  $T_{\text{eff}}$ ) are adopted directly from TIC v8.2 (Stassun et al. 2019) without applying specialized M-dwarf relations (e.g., Mann et al. 2015). Distances are cross-validated with Gaia DR3 parallaxes (Gaia Collaboration 2023). For mid-M dwarfs, TIC radii carry systematic uncertainties of 10–20% (Stassun et al. 2019), propagating directly to planetary radii as  $\sigma_{R_p}/R_p \approx \sigma_{R_{\star}}/R_{\star}$ . Consequently, a candidate reported as  $R_p = 0.8 R_{\oplus}$  may range from  $0.65\text{--}0.95 R_{\oplus}$ . Spectroscopic refinement of  $R_{\star}$  is required before definitive sub-Earth classification. Spectral type assignments (M3–M6) are based on TIC  $T_{\text{eff}}$ ; uncertainties of  $\pm 100\text{--}200$  K can shift classification by one subtype.

Detrending uses Gaussian Process regression via `celerite2` (Foreman-Mackey et al. 2017) with a two-component kernel: a stochastic harmonic oscillator (SHOTerm, quasi-periodic) for stellar variability and a Matérn-3/2 term for long-term trends. The primary timescale  $\rho$  is adaptive (0.3–5.0 d) with a hard floor at 0.3 d to preserve transit signals. For GP convergence failures, the pipeline falls back to biweight detrending via `wotan` (Hippke et al. 2019). Stellar flares—common in M-dwarfs—are handled through the asymmetric sigma-clipping ( $4\sigma$  above median): isolated positive excursions are clipped while preserving the symmetric transit dips. The GP’s long timescale ( $> 0.3$  d) further prevents flare contamination of the baseline, as flares typically last minutes to hours. Detrended sectors are stitched chronologically, yielding multi-sector lightcurves spanning 700–2 600 days with  $\sim 50\,000\text{--}200\,000$  measurements per target.

### 3.2. Transit Detection

Transit detection uses TLS (Hippke & Heller 2019) with quadratic limb-darkening coefficients computed for the TESS bandpass from Claret (2017). Key parameters: period range  $0.5 < P < \min(0.7B, 100)$  days; detection threshold  $\text{SDE}_{\text{eff}} \geq 7.0$ ; iterative search for up to 6 planets per system. The effective SDE is computed as  $\text{SDE}_{\text{eff}} = \text{SDE}_{\text{TLS}} / \sqrt{\beta_{\text{rn}}}$ , where  $\text{SDE}_{\text{TLS}}$  is the raw output of the `transitleastsquares` library and  $\beta_{\text{rn}} = (\sigma_{\text{binned}}/\sigma_{\text{white}})^2 \geq 1$  is the red-noise variance ratio of Pont et al. (2006) that accounts for time-correlated noise. This penalization is applied as a custom post-processing step to the standard TLS output. All subsequent SDE values in this paper refer to  $\text{SDE}_{\text{eff}}$ .

For long baselines ( $B > 500$  d), a two-phase ‘‘Scout/Sniper’’ strategy reduces computation by a factor scaling with  $N_{\text{raw}}/N_{\text{bin}}$  (typically 2–5 $\times$  for the survey baselines): Scout phase bins the lightcurve (reducing  $N$  by  $\sim 5\times$ ) and searches over the full period grid with a relaxed threshold ( $\text{SDE} \geq 4.5$ ); Sniper phase refines only the Scout detections on unbinned data within  $\pm 10\%$  of Scout periods. The speedup scales with  $N_{\text{raw}}/N_{\text{bin}}$ , since TLS computation is  $O(N \times M)$  where  $M$  is the period grid size.

#### 3.2.1. Harmonic Correction

Harmonic aliasing occurs when TLS detects  $2P$  or  $3P$  instead of the true period  $P$ . Three evidence modes address this, each targeting a distinct aliasing signature:

**Mode A (equal-depth secondary):** inspired by the Kepler Model-Shift Uniqueness Test (Twicken et al. 2018) and the Robovetter (Coughlin et al. 2016; Thompson et al. 2018), a per-epoch matched filter measures event depth at phase 0.5 using only epochs with  $\geq 5$  TESS data points and the mean in-transit flux within  $\pm T_{\text{dur}}/2$ . A depth ratio exceeding 0.4 identifies a  $2P$  alias, since no planetary secondary exceeds  $\sim 2\%$  of the primary depth (Santerne et al. 2013). **Mode B (odd-even depth mismatch):** if  $|\delta_{\text{odd}} - \delta_{\text{even}}| > 3\sigma$  (Batalha et al. 2013), alternating transit depths indicate a  $2P$  alias of an eclipsing binary. **Mode C (equal-depth thirds):** equal-depth events at phases  $1/3$  and  $2/3$  (ratio  $> 0.4$ ) identify  $3P$  aliases; no single planet produces three equidistant transit-like events at phases 0,  $1/3$ , and  $2/3$  with comparable depths. For depth ratios  $> 0.8$  (Modes A/C), the SNR requirement is waived following the Kepler Robovetter (Thompson et al. 2018); for ratios 0.4–0.8,  $\text{SNR} > 3$  is required. The pipeline resolves the period by re-running TLS at candidate sub-harmonics ( $P/2, P/3, P/4$ ) with an evidence-dependent adaptive threshold:

- Mode A (equal-depth secondary,  $2P$  alias):  $\text{SDE} > 0.3 \times \text{SDE}_{\text{orig}}$ ;
- Mode B (odd-even  $> 3\sigma$ ,  $2P$  alias):  $\text{SDE} > 0.8 \times \text{SDE}_{\text{orig}}$ ;
- Mode C (equal-depth thirds,  $3P$  alias):  $\text{SDE} > 0.3 \times \text{SDE}_{\text{orig}}$ ;
- No physical evidence: no resolution attempted (SDE ratio alone is not diagnostic).

**Transit count correlation:** if  $P_2/P_1 \approx N$  and  $N_{\text{tr}}(P_1)/N_{\text{tr}}(P_2) \approx N$  within 10%, the longer period is flagged as harmonic. To preserve true 2:1 mean motion resonance (MMR) systems (Fabrycky et al. 2014), the algorithm does not resolve to a period already accepted for the same target.

### 3.3. Signal Validation Cascade

Each TLS detection undergoes a cascade of 18 diagnostic checks (13 REJECT, 1 METRIC, 4 LOG) within the detection mod-

ule before reaching statistical vetting. Table 4 summarizes these checks; the key diagnostics are described below.

**Table 4.** Signal validation cascade: 18 diagnostic checks.

#	Check	Type	Threshold
1	Signal polarity	R	$\text{SNR} \leq 0$
2	Period aliases	R	$P \approx 0.5, 1.0, 13.7$ d
3	Sub-harmonics	R	$P/n$ of accepted cand.
4	Transit count corr.	R	$N_{\text{tr}}$ ratio $\approx N$
5	Dynamical stability	R	$\Delta < 3.5 R_{\text{Hill}}$
6	Centroid offset	R	$> 5\sigma$
7	Secondary eclipse	R	Depth ratio $> 0.10$
8	Odd-even depth	R	$> 3\sigma$
9	Duration plausibility	R	$T_{\text{obs}}/T_{\text{exp}} \notin [0.3, 3.0]$
10	NTL spike test	R	Median/mean $< 0.20$
11	SWEET variability	R	$A_{\text{ratio}} < f(\delta)$
12	OOT scatter gate	R	MAD $> 2\times$ expected
13	Detrend. response	R	Pre/post-GP $> 2.5$
14	Depth consistency	M	4-layer diagnostic
15–18	Transit parameters	L	Logged for catalog

**Notes.** R = REJECT (13 checks), M = METRIC (1; recorded but not rejection), L = LOG (4; audit trail). Checks are applied sequentially; a REJECT terminates the cascade for the current candidate.

**Signal polarity.** As the first check, candidates with  $\text{SNR} \leq 0$  are rejected as inverted signals—physically impossible for a transit, which must produce a flux decrease. On active M-dwarfs (MAD  $> 2500$  ppm), correlated stellar variability can inflate SDE while producing negative SNR (upward bump); this check fires before all other diagnostics.

**Instrumental rejection.** Candidates at known systematic periods are rejected: TESS orbital period ( $13.7 \pm 2\%$  d), Earth rotation aliases (0.5 and 1.0 d within  $\pm 2\%$ ; Fausnaugh et al. 2018). A spike test inspired by the Kepler Robovetter Not-Transit-Like (NTL) metric (Coughlin et al. 2016; Thompson et al. 2018) rejects instrumental artifacts (momentum dumps, cosmic rays) when the ratio of median to mean in-transit depth falls below 0.20 ( $\geq 4$  in-transit points required): real transits depress all in-transit points uniformly (ratio  $\approx 1$ ), while isolated outliers affect only the mean (ratio  $\approx 0$ ).

**Eclipsing binary rejection.** Odd-even depth comparison ( $> 3\sigma$ ) rejects EBs (Batalha et al. 2013). Centroid analysis ( $> 5\sigma$  offset) rejects blends (Bryson et al. 2013). Secondary eclipse detection (depth ratio  $> 0.10$ ) rejects EBs, with the SNR requirement waived for ratio  $> 0.15$  (Santerne et al. 2013); for multi-planet candidates with near-2:1 period ratios, secondary rejection is bypassed when  $P/2$  matches an accepted candidate (within 3%), preventing false rejection from transit masking artifacts. Dynamical stability is checked for multi-planet systems ( $\Delta > 3.5$  mutual Hill radii; Gladman 1993; Chambers et al. 1996).

**Stellar rotation estimation.** Rotation periods are estimated via Generalized Lomb-Scargle periodogram (Zechmeister & Kürster 2009) on pre-GP flux (FAP  $< 5\%$ ), with Earth rotation and TESS orbital aliases vetoed. The relaxed FAP (from 0.1%) maximizes  $P_{\text{rot}}$  sensitivity on active M-dwarfs; false assignments are mitigated by requiring phase coherence  $< 0.75$  before rejection.

**Stellar variability rejection.** Short-period candidates ( $P < 2 P_{\text{rot}}$ , or  $P < 15$  d when  $P_{\text{rot}}$  is unavailable) are tested through three complementary diagnostics on pre-GP flux: (1) a sinusoidal variability test (SWEET, after the Kepler Robovetter; Thompson et al. 2018; Kunitomo et al. 2025) fits sinusoids at  $P$ ,

$P/2$ ,  $2P$  per TESS segment, rejecting when the amplitude ratio  $A_{\text{ratio}} = \delta / (2A_{\text{sine,median}})$  falls below a depth-scaled threshold  $\max(1.5, 2.5(1 - e^{-\delta/1000}))$ ; (2) a Folded OOT Scatter Gate rejects when binned out-of-transit MAD exceeds both  $2\times$  expected noise and 30% of depth; (3) a Detrending Response Test rejects when depth ratio pre-GP/post-GP  $> 2.5$ , indicating variability absorbed by GP.

**Depth consistency.** A four-layer diagnostic addresses variability at all periods: Layer 1 rejects phase coherence  $< 0.5$ ; Layer 2 rejects inter-sector depth coefficient of variation (CV)  $> 0.5$ ; Layer 3 rejects  $P \approx P_{\text{rot}}$  harmonics ( $P_{\text{rot}}/3$ ,  $P_{\text{rot}}/2$ ,  $P_{\text{rot}}$ ,  $2P_{\text{rot}}$ ,  $3P_{\text{rot}}$ ) with phase coherence  $< 0.75$ ; Layer 4 rejects sector CV  $> 0.70$  combined with phase coherence  $< 0.80$ . Layers 1–2 are SNR-gated (bypassed when per-epoch SNR  $< 2.0$ ).

**Quality flag system.** Following the Kepler Robovetter (Thompson et al. 2018) and its TESS adaptation LEO-Vetter (Kunimoto et al. 2025), candidates receive a quality flag: HIGH\_CONFIDENCE (default) or MARGINAL\_ACTIVE\_STAR (median absolute deviation MAD  $> 5\,000$  ppm, planet number  $> 1$ , SDE  $< 20$ ). Marginal candidates bypass statistical vetting but are retained for human review.

**Harmonic nest cleanup.** On active M-dwarfs, TLS can produce multiple false candidates per star from BY Dra variability harmonics. A post-detection cleanup analyzes all candidates per target simultaneously via two tests: (1) cross-masking (Thompson et al. 2018; Coughlin et al. 2016)—for each candidate pair (A, B) with  $\text{SDE}_A > \text{SDE}_B$ , the transits of A are masked ( $\pm 1.5 \times T_{\text{dur}}/2$ ) and the residual depth of B is measured; if residual depth  $< 50\%$  of the original, B is flagged as dependent on A; (2) system parsimony—the maximum number of plausible detections is capped by stellar activity (MAD  $< 1500$  ppm: 5; 1500–3000: 3; 3000–5000: 2;  $> 5000$ : 1), with a +2 bonus when best SDE  $> 20$  and SNR  $> 5$ . These thresholds were calibrated empirically on the 10 validation systems (Sect. 5): L 98-59 (MAD = 1 674 ppm, 3 planets) passes within the cap; TOI-700 (MAD = 3 615 ppm, 4 planets) is protected by the SDE  $> 18$  safety guard. Cross-masking evidence takes priority over parsimony. Systems with SDE  $> 18$  or SNR  $> 7$  bypass the parsimony test to protect genuine multi-planet systems.

### 3.4. Candidate Validation

Candidates passing the signal validation cascade are assessed along two complementary axes: *astrophysical validation* (this section) determines whether the signal is consistent with a planetary transit rather than a false positive; *signal reliability* (Sect. 3.5) quantifies whether the detection is statistically distinguishable from the host star’s noise floor. At the noise frontier, signal reliability is the primary classification driver.

#### 3.4.1. Statistical Vetting and Parameter Fitting

Candidates passing the signal validation cascade undergo false-positive screening via TRICERATOPS (Giacalone & Dressing 2020; Giacalone et al. 2021), which computes the false positive probability (FPP) and nearby false positive probability (NFPP). TRICERATOPS evaluates astrophysical false-positive scenarios (blends, BEBs, eclipsing binaries) but does not assess instrumental systematics or stellar variability—the primary contaminants on active M-dwarfs. This motivates the 18-check signal

validation cascade (Sect. 3.3) applied *before* TRICERATOPS. Classification thresholds follow Giacalone et al. (2021): FPP  $< 1.5\%$  and NFPP  $< 0.1\%$  for statistical validation; FPP  $\geq 50\%$  or NFPP  $> 80\%$  for rejection. Intermediate cases with clean observational diagnostics proceed to Gaia physical verification (Sect. 3.4.2). Table 5 lists all disposition categories.

Candidates passing vetting undergo Markov Chain Monte Carlo (MCMC) parameter fitting using emcee (Foreman-Mackey et al. 2013) with batman transit models (Kreidberg 2015), fitting  $R_p/R_*$ , impact parameter  $b$ , and  $T_0$ . Table 5 summarizes all disposition categories assigned across the three validation phases.

**Table 5.** Pipeline disposition categories across validation phases.

Disposition	Criteria
<i>Statistical vetting (Sect. 3.4.1)</i>	
LIKELY_PLANET	FPP $< 50\%$ : probable planet
PENDING_VERIF. <sup>a</sup>	NFPP 10–80%, observations clean
GRAZING_CAND.	Impact parameter $b > 0.9$
LIKELY_EB	Secondary ratio $> 0.10$ , prob_EB $> 15\%$ , or duration anomaly
AMBIGUOUS	FPP $\geq 50\%$ , NFPP $< 10\%$
MARGINAL <sup>b</sup>	MAD $> 5000$ ppm, pl.# $> 1$ , SDE $< 20$
FALSE_POS.	NFPP $\geq 80\%$ or centroid $> 5\sigma$
<i>Signal reliability (Sect. 3.5)</i>	
Tier	Signal reliability tier (1/2/3)
<i>Gaia physical verification (Sect. 3.4.2)</i>	
PLANET_CAND.	0 contaminants, RUWE $< 1.4$
PC_HEB_CAUT.	0 contaminants, RUWE $\geq 1.4$
NEEDS_HR_IMG	$\geq 1$ contaminant, RUWE $< 1.4$
FALSE_POS.	$\geq 1$ contaminant, RUWE $\geq 1.4$

**Notes.** PENDING and LIKELY\_PLANET candidates proceed to Gaia verification. <sup>a</sup>PENDING\_PHYSICAL\_VERIFICATION: FPP  $\geq 50\%$  but observations clean; Gaia can exclude BEB at  $\rho > 0.4''$  and upgrade the candidate. <sup>b</sup>MARGINAL\_ACTIVE\_STAR; bypasses TRICERATOPS.

#### 3.4.2. Physical Verification via Gaia DR3

Background eclipsing binaries (BEB) are the dominant false-positive scenario for faint M-dwarf hosts. Gaia DR3 directly tests BEB hypotheses (Fig. 1) by querying sources within  $30''$  brighter than  $R_{p,\text{max}}$ , the faintest contaminant capable of producing the observed depth  $\delta$ :

$$R_{p,\text{max}} = T_{\text{mag}} - 2.5 \log_{10}(\delta) \quad (1)$$

where the contaminant search uses Gaia  $R_p$ -band photometry (630–1000 nm) rather than the broadband  $G$  magnitude, since Gaia  $R_p$  closely matches the TESS bandpass (600–1000 nm) for M-dwarf spectral energy distributions (Fabricius et al. 2021). For mid-M dwarfs,  $T_{\text{mag}}$  and Gaia  $R_p$  agree to within  $\sim 0.1$ – $0.2$  mag, making  $T_{\text{mag}}$  a suitable proxy; the residual offset is anti-conservative (slightly underestimating  $R_{p,\text{max}}$ ), but smaller than the typical magnitude margin between the brightest contaminant and the threshold (Table A.5). Zero contaminants with RUWE  $< 1.4$  (Lindgren et al. 2021) yields PLANET\_CANDIDATE;  $\geq 1$  contaminant yields NEEDS\_HR\_IMAGING. Only PENDING and LIKELY\_PLANET candidates enter verification. For LIKELY\_PLANET candidates (FPP  $< 50\%$ ), TRICERATOPS has already integrated BEB priors via TRILEGAL; Gaia contaminants therefore do not downgrade these candidates but prompt a recommendation for high-

resolution imaging. Gaia cannot resolve companions  $<0.4''$ ; HR imaging remains required for confirmation.

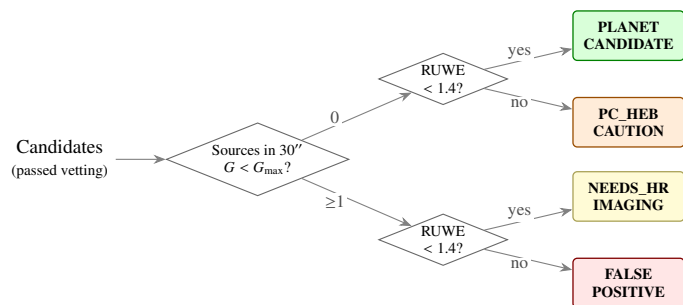


**Fig. 1.** Gaia DR3 physical verification decision tree. Candidates passing statistical vetting are classified based on aperture contamination ( $G_{\max}$  from Eq. 1) and astrometric quality (RUWE).

### 3.5. Signal Reliability Framework

The  $SDE \geq 7$  detection threshold has a  $\sim 17\%$  empirical false alarm rate on M3–M6 dwarfs (Sect. 7.3), motivating a per-candidate reliability assessment beyond the binary detected/not-detected classification. Three independent empirical tests probe complementary aspects of signal robustness:

- 1. Circular shift FAR** (Jenkins et al. 2002): per-sector time shifts destroy inter-sector transit coherence while preserving stellar variability. A TIC is flagged if the scrambled lightcurve produces  $SDE \geq 7$  candidates through the full pipeline.
- 2. Lightcurve inversion** (Coughlin et al. 2016): reflecting the flux ( $f_{\text{inv}} = 2 - f$ ) converts transit dips to bumps; any  $SDE \geq 7$  detection in the inverted data establishes the per-star noise floor. A candidate is flagged if  $SDE_{\text{inv}} \geq 0.8 \times SDE_{\text{real}}$ .
- 3. Fourier phase scrambling** (Timmer & König 1995): per-sector FFT with randomized phases preserves the power spectrum but destroys all waveform coherence. Per-star false alarm probability (FAP) is estimated from  $N = 20$  scrambles (resolution  $\Delta\text{FAP} = 5\%$ ).

Combined results classify each candidate into one of three signal reliability tiers (Table 6). The astrophysical nature assessment (BEB exclusion, FPP, centroid, odd/even) is reported separately from signal reliability.

**Table 6.** Signal reliability tier definitions.

Tier	Signal criteria
1 (High Robustness)	No FAR flag AND $SDE_{\text{inv}} < 7$
2 (Moderate Robustness)	Flagged by one test only
3 (Noise-Susceptible)	Flagged by both tests

**Notes.** FAR flag = host TIC produced  $\geq 1$  false alarm candidate on circularly shifted lightcurve.  $SDE_{\text{inv}}$  = best SDE from inverted lightcurve (noise floor). Fourier FAP refines the initial classification:  $\text{FAP} \geq 25\%$  downgrades one tier. Monotransit candidates (single transit epoch) are excluded from the tier system. Detailed results and per-candidate tier assignments are presented in Sect. 7.3.

## 4. Injection-Recovery Tests

The pipeline detection sensitivity is characterized through end-to-end injection-recovery tests on activity-stratified representative hosts. The 121-star sample spans a wide range of photometric scatter ( $\sigma_{\text{MAD}} = 1204\text{--}10801$  ppm), and detection sensitivity varies strongly with stellar activity. To capture this dependence, three archetype hosts were selected from the tercile boundaries of the sample scatter distribution: a photometrically calm star (TIC 402375302;  $\sigma_{\text{MAD}} = 1519$  ppm), a median-activity star (TIC 186664624;  $\sigma_{\text{MAD}} = 4559$  ppm), and an active star (TIC 129781877;  $\sigma_{\text{MAD}} = 5870$  ppm). Each archetype received 100 injections using four-dimensional Sobol quasi-Monte Carlo (QMC) sampling ( $R_p$ ,  $P$ ,  $b$ ,  $T_0$ ; Ment & Charbonneau 2023). Unlike occurrence rate studies requiring dense Monte Carlo sampling across the parameter grid, this injection-recovery campaign characterizes detection degradation across activity regimes, adopting the sparse sampling approach of Ment & Charbonneau (2023) with  $\pm 16\%$  Poisson uncertainty per radius-period bin (10 injections/bin).

### 4.1. Methodology

Synthetic transits were generated with *batman* (Kreidberg 2015) and injected into raw lightcurves *before* any preprocessing. Each injection was processed through the full pipeline—GP detrending followed by TLS detection with Scout/Sniper optimization (Sect. 3.2)—called as subprocesses to ensure identical treatment to the discovery pipeline. The injection parameters were:

- Planet radius:  $R_p \in [0.5, 4.0] R_{\oplus}$ , log-uniform
- Orbital period:  $P \in [0.5, 100]$  d, log-uniform
- Impact parameter:  $b \sim \mathcal{U}(0, 0.9)$ ; eccentricity  $e = 0$  (circular orbits)
- Epoch:  $T_0 \sim \mathcal{U}(t_{\min}, t_{\min} + P)$
- Limb darkening: quadratic coefficients for the TESS bandpass from Claret (2017), interpolated per stellar  $T_{\text{eff}}$
- Stellar parameters:  $R_{\star}$  and  $M_{\star}$  from TIC for each target

A signal was considered recovered if  $SDE \geq 7.0$  and  $\min_k |P_{\text{found}} - P_k|/P_k < 0.002$ , where  $P_k \in \{nP_{\text{inj}}, P_{\text{inj}}/n\}$  for  $n \in \{1, 2, \dots, 7\}$ , following Ment & Charbonneau (2023). The 0.2% tolerance ensures precise period matching; the harmonic set accounts for TLS phase-folding degeneracies at integer multiples of the true period (Hippke & Heller 2019). Fractional-ratio aliases (e.g.,  $2P/3$ ,  $4P/5$ ) are excluded for consistency with the literature; their inclusion would increase recovery rates by  $\sim 2$  percentage points.

The period range extends to  $P = 100$  d, covering the full accessible detection space including extended periods ( $P = 20\text{--}100$  d) where sparse coverage limits detection. These tests measure *detection* completeness only. The vetting stage (TRICER-ATOPS, centroid analysis) is excluded because it requires pixel-level data unavailable for synthetic injections; vetting produced zero false negatives across 16 validated planets (Sect. 5).

### 4.2. Activity-stratified completeness

Table 7 summarizes recovery rates for three activity archetypes. The calm archetype achieves 56.0% overall recovery (56/100; 95% Wilson CI [46, 65%]), the median-activity archetype recovers 28.0% (28/100; CI [20, 37%]), and the active archetype recovers only 18.0% (18/100; CI [12, 27%])—a total degradation

**Table 7.** Activity-stratified injection-recovery completeness (100 Sobol QMC injections per host). Wilson 95% CIs in brackets.

	Calm <sup>a</sup>	Median <sup>b</sup>	Active <sup>c</sup>
<b>Overall</b>	<b>56/100 = 56.0%</b> [46, 65]%	<b>28/100 = 28.0%</b> [20, 37]%	<b>18/100 = 18.0%</b> [12, 27]%
<i>By planet radius</i>			
$R_p < 1.0 R_\oplus$	4/33 = 12.1%	0/35 = 0.0%	0/34 = 0.0%
$1.0 \leq R_p < 2.0 R_\oplus$	23/33 = 69.7%	7/31 = 22.6%	4/34 = 11.8%
$R_p \geq 2.0 R_\oplus$	29/34 = 85.3%	21/34 = 61.8%	14/32 = 43.8%
<i>By orbital period</i>			
$P < 5$ d	32/44 = 72.7%	20/43 = 46.5%	13/43 = 30.2%
$5 \leq P < 20$ d	15/25 = 60.0%	6/28 = 21.4%	5/27 = 18.5%
$P \geq 20$ d	9/31 = 29.0%	2/29 = 6.9%	0/30 = 0.0%
Min. recovered $R_p$	0.77 $R_\oplus$	1.34 $R_\oplus$	1.76 $R_\oplus$
SDE $\geq 7$ , wrong $P$	3	32	0

**Notes.** <sup>a</sup>TIC 402375302,  $\sigma_{\text{MAD}} = 1\,519$  ppm. <sup>b</sup>TIC 186664624,  $\sigma_{\text{MAD}} = 4\,559$  ppm. <sup>c</sup>TIC 129781877,  $\sigma_{\text{MAD}} = 5\,870$  ppm. Wrong  $P$ : SDE  $\geq 7$  candidate but no harmonic alias match within 0.2%.

factor of  $3.1\times$  from calm to active, consistent with the  $\beta \approx 1.5$ – $1.6$  reported by Yaptangco et al. (2025) for active vs. inactive M-dwarfs.

Recovery depends strongly on both planet size and orbital period. For the calm archetype, planets with  $R_p \geq 2.0 R_\oplus$  are recovered at 85% (29/34) across all periods, and short-period planets ( $P < 5$  d) at 73% (32/44). Sub-Earths ( $R_p < 1.0 R_\oplus$ ) are recovered at 12% (4/33), with the smallest recovered planet at  $0.77 R_\oplus$ . At extended periods ( $P \geq 20$  d), completeness drops to 29% (9/31) even for the calm archetype; 3 injections produced wrong-period detections (SDE  $\geq 7$  at non-matching periods).

For the median archetype, no sub-Earth was recovered (0/35), the minimum recovered radius rises to  $1.34 R_\oplus$ , and long-period recovery ( $P \geq 20$  d) drops to 7% (2/29). Stellar variability is the dominant factor: 32 of 100 injections produced SDE  $\geq 7$  candidates at incorrect periods, with 19 of these locking onto the stellar rotation signal at  $P \approx 0.54$  d. This “variability confusion” mechanism—where TLS preferentially detects the highest-amplitude periodic signal—explains the discrepancy between the 100% pipeline validation on known systems (Sect. 5)—which were pre-selected as planet hosts—and the lower injection recovery rates on representative M3–M6 targets.

The active archetype ( $\sigma_{\text{MAD}} = 5\,870$  ppm) confirms these trends at the extreme end: overall recovery drops to 18% (18/100; CI [12, 27]%), no planet below  $1.76 R_\oplus$  is recovered, and no recovery occurs beyond  $P = 14.8$  d. Although 65 of 100 injections yielded maximum TLS SDE  $\geq 7$ , none of these false-period detections survived the vetting checks (0 wrong- $P$  candidates). The full calm–median–active sequence yields a  $3.1\times$  degradation factor at approximately constant  $R_\star$  ( $0.328$ – $0.340 R_\odot$ ).

The calm archetype achieves  $\geq 50\%$  recovery for  $R_p \geq 1.0 R_\oplus$  at  $P < 10$  d and for  $R_p \geq 2.0 R_\oplus$  at all periods, while the active archetype is confined to  $R_p \geq 2.0 R_\oplus$  at  $P < 5$  d. Per-bin recovery fractions (Table 7) are based on 25–44 injections per bin; the corresponding Wilson 95% confidence intervals are  $\pm 10$ – $16\%$  (absolute), comparable to the  $\sim 100$  injections per archetype used by Ment & Charbonneau (2023). These uncertainties are dominated by the Sobol sampling density rather than by pipeline stochasticity, and do not affect the main conclusions (calm-to-active degradation, sub-Earth detection threshold) which are derived from the full 100-injection aggregates with tighter constraints (Table 7, top row).

## 5. Pipeline Robustness

Injection tests characterize sensitivity to synthetic signals; validation on *real* planetary systems provides a complementary robustness check. The full detection and vetting chain was applied blindly to 10 M-dwarf systems with confirmed transiting planets that meet the sample selection criteria ( $\geq 3$  TESS sectors): L 98-59 (Kostov et al. 2019) (3 planets), TOI-700 (Gilbert et al. 2020) (4 planets including HZ planet d), Gliese 12 (Dholakia et al. 2024) (HZ planet b), GJ 357 (Luque et al. 2019), GJ 3473 (Kemmer et al. 2020), GJ 486 (Trifonov et al. 2021), TOI-406, TOI-782, TOI-6086 (Barkaoui et al. 2024), and LP 791-18 (Crossfield et al. 2019) (2 TESS-detectable planets). This test achieved **100% recovery** (16/16 TESS-detectable planets) with **zero false positives** (Table 8). Detailed per-system analysis is provided in Appendix C.

**Table 8.** Validation summary: 10 systems, 16 TESS-detectable planets, 100% recovery.

System	SpT	Pl.	HZ	Gaia	Status
L 98-59	M3V	3/3	—	0	PLANET_CAND
TOI-700	M2V	4/4	d	2–5	NEEDS_HR
Gliese 12	M4V	1/1	b	0	PLANET_CAND
GJ 357	M2.5V	1/1	—	2	NEEDS_HR
GJ 3473	M4V	1/1	—	0	PLANET_CAND
GJ 486	M3.5V	1/1	—	0	PLANET_CAND
TOI-406	M4V	1/1	—	1	NEEDS_HR
TOI-782	M3V	1/1	—	1	NEEDS_HR
TOI-6086	M3.5V	1/1	—	1	NEEDS_HR
LP 791-18	M5V	2/2 <sup>†</sup>	—	1–2	NEEDS_HR
<b>Total</b>		<b>16/16</b>	<b>2</b>		<b>0 FP</b>

**Notes.** Gaia = contaminants within  $30''$ . <sup>†</sup>LP 791-18 d excluded (Spitzer discovery, Peterson et al. 2023). All validation planets classified as NEEDS\_HR\_IMAGING were confirmed using speckle or AO imaging in their discovery papers (Gilbert et al. 2020; Luque et al. 2019; Barkaoui et al. 2024; Peterson et al. 2023).

The validation demonstrates several important results. Period accuracy exceeds 99.99% for 15 of 16 detections; L 98-59 d shows a 0.94% offset attributable to iterative planet masking (Table C.2). Both HZ validation planets (TOI-700 d and Gliese 12 b) were correctly identified. The NEEDS\_HR\_IMAGING classification is the majority outcome (10 of 16 planets), consistent with the requirements from the original discovery papers. Validation targets satisfy the sector criterion ( $\geq 3$  sectors) but not necessarily the M3–M6 spectral type restriction (e.g., TOI-700 is M2V). No M6 validation targets meeting the sample criteria exist. LP 791-18 (M5V,  $T_{\text{eff}} = 2949$  K) validates detection on late M-dwarfs, though its magnitude ( $T_{\text{mag}} = 13.56$ ) exceeds the sample limit. Candidates around M6 hosts remain less robustly validated than earlier types. The signal reliability tier system (Sect. 3.5) was not formally applied to validation targets: these hosts have photometric scatter well below the noise frontier (median MAD  $\approx 1\,800$  ppm versus  $4\,800$  ppm for the survey sample) and detection SDE = 18–65 (versus 7–12 for survey candidates), so the tier system—designed to discriminate at the noise frontier—would trivially assign Tier 1 to all validation hosts, providing no calibration information at the SDE and noise levels where classification is ambiguous.

Phase-folded lightcurves are shown in Figs. 2 and 3.

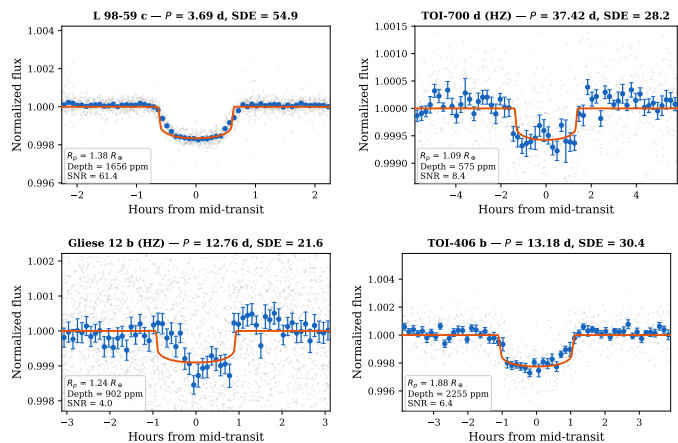


**Fig. 2.** Validation lightcurves (1/2). **Top row:** L 98-59 c, TOI-700 d (HZ). **Bottom row:** Gliese 12 b (HZ), TOI-406 b.

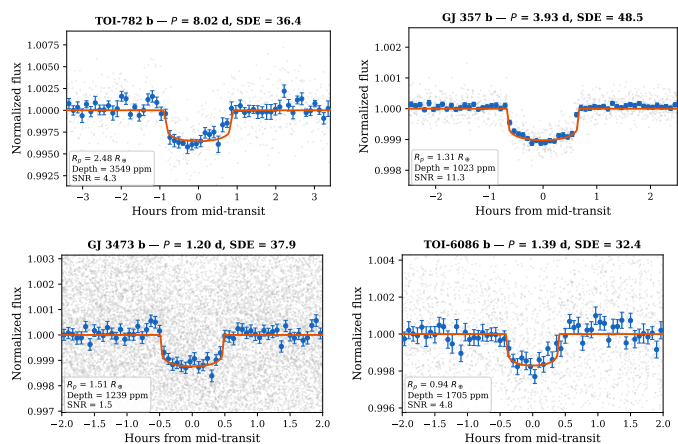


**Fig. 3.** Validation lightcurves (2/2). **Top row:** TOI-782 b, GJ 357 b. **Bottom row:** GJ 3473 b, TOI-6086 b.

## 6. Limitations and Failure Modes

Characterizing pipeline limitations is essential for interpreting detection statistics and occurrence rate estimates. The sample selection (Table 2) was designed to mitigate several known failure modes, but residual limitations remain.

**Photometric quality.** Ultra-bright stars ( $T_{\text{mag}} < 8$ ) exhibit severe red noise rendering transit detection unreliable; testing on AU Mic ( $T_{\text{mag}} = 6.8$ ; Plavchan et al. 2020) yielded 0/3 planet recoveries despite 3 sectors and deep transits ( $\sim 2000$  ppm), with a red noise factor  $\beta_{\text{rn}} = 10.0$  (the survey maximum). Ultra-faint stars ( $T_{\text{mag}} > 13$ ) suffer photon-limited noise: testing on LP 890-9 ( $T_{\text{mag}} = 14.3$ , 4 sectors) recovered planet b at the correct period ( $P = 2.73$  d,  $\text{SDE} = 18.5$ ) but missed the HZ planet c ( $P = 8.46$  d), whose discovery required 614 hours of ground-based SPECULOOS observations (Delrez et al. 2022). Both failure modes are mitigated by sample selection ( $T_{\text{mag}} = 8\text{--}12.5$ ), though LP 890-9 demonstrates that short-period planets with deep transits remain detectable beyond this range.

**Period blind spots.** Periods near TESS systematics—0.5 d, 1.0 d (Earth rotation; Fausnaugh et al. 2018), and 13.7 d (spacecraft orbit)—are rejected by the vetting cascade (Sect. 3.3), creating blind spots where genuine ultra-short-period planets would be missed. The harmonic breaker (Sect. 3.2.1) corrects sub-harmonic aliases ( $P/2$ ,  $P/3$ ) but requires sufficient phase coverage to distinguish the true period; with sparse coverage ( $\leq 5$

sectors), this correction can fail (e.g., L 98-59 c detected at  $P/2$  under 3-sector conditions).

**Scout/Sniper limitations.** The two-phase optimization introduces three potential failure modes: (1) Scout threshold losses (signals with  $4.5 < \text{SDE}_{\text{binned}} < 7$  may be missed by Scout); (2) Sniper window misses for strong aliases outside  $\pm 10\%$  of the Scout period; (3) ultra-short transit dilution for  $P < 1$  d around  $R_{\star} < 0.15 R_{\odot}$  hosts where transit duration approaches the binning cadence. These losses are included in the injection-recovery completeness (Sect. 4), which provides an end-to-end measure of detection sensitivity including Scout/Sniper effects.

**Stellar activity.** Active M-dwarfs with elevated red noise can push marginal detections below threshold. The AU Mic limit test demonstrates this: despite 3 sectors and deep transits ( $\sim 2000$  ppm), all known planets were missed due to extreme stellar variability. The pipeline deliberately prioritizes sample purity over completeness on active stars—a trade-off that reduces the risk of false positives at the cost of missing some genuine planets.

**Sparse temporal coverage.** This is the dominant limitation. The survey targets have 3–10 sectors (median 4), providing only  $\sim 80\text{--}160$  d of photometry spread over baselines of 700–2600 d. This sparse coverage has two consequences: (1) planets with  $P > 20$  d produce  $\leq 3$  transit events, insufficient for robust phase-folding and period determination; (2) the gap-dominated window function generates period aliases. Validation tests quantify the impact: restricting 4 known systems (L 98-59, TOI-700, Gliese 12, TOI-406) to 3 sectors recovers only 2/9 planets (22%), with all 5 planets at  $P > 10$  d missed regardless of depth. With full sector coverage, the same systems achieve 9/9 (100%). Detection capability therefore scales directly with sector count, and as the “newly enabled” targets accumulate additional TESS sectors, completeness at longer periods will improve.

## 7. Results

### 7.1. Survey Statistics

Table 9 summarizes the detection statistics from the complete survey.

**Table 9.** Survey detection statistics for the 121-star M3–M6 sample.

Category	Count	Fraction
Total stars analyzed	121	100%
No detection ( $\text{SDE} < 7$ )	98	81.0%
With transit signals ( $\text{SDE} \geq 7$ )	23	19.0%
<b>Surviving candidates</b>	<b>20</b>	<b>16.5%<sup>a</sup></b>

**Notes.** <sup>a</sup>Fraction of total sample (121 stars).

Transit-like signals ( $\text{SDE} \geq 7$ ) were detected in 19.0% of targets (23/121), producing 33 candidates after harmonic nest cleanup. After vetting, 13 candidates were rejected (9 LIKELY\_EB, 3 FALSE\_POSITIVE, 1 GRAZING\_CANDIDATE), yielding **20 surviving transit-like signals across 16 systems** (Table 10). The 39% rejection rate (13/33) is dominated by eclipsing binary scenarios (9 LIKELY\_EB), consistent with the high BEB incidence expected from TESS’s large pixel scale ( $21''$ ) for faint M-dwarf hosts (Sullivan et al. 2015). All 20 surviving signals received the HIGH\_CONFIDENCE quality flag; no MARGINAL\_ACTIVE\_STAR candidate survived to the final classification. None have prior TOI designations in ExoFOP-TESS or

the NASA Exoplanet Archive (query date: 28 February 2026). Exhaustive per-candidate parameters, host star properties, and rejected candidate details are provided in Appendix A.

## 7.2. Candidate Classification

The 20 signals are classified along two complementary axes: *physical verification* (PLANET\_CANDIDATE or NEEDS\_HR\_IMAGING, Sect. 3.4.2) determines whether astrophysical false positives are excluded; *signal reliability* (Tier 1–3, Sect. 3.5) quantifies the risk that stellar noise produces a signal of comparable strength. At the stellar noise frontier, signal reliability is the primary classification axis; physical verification determines imaging priorities. Table 10 presents the disposition of all detected signals after TRICERATOPS vetting and Gaia DR3 physical verification.

**Table 10.** Final classification of detected transit signals. 23 TICs produced 33 candidates after harmonic nest cleanup; some TICs contribute candidates to multiple categories.

Category	Cand.	Sys. <sup>a</sup>
<i>Surviving candidates</i>		
PLANET_CANDIDATE	9	8
NEEDS_HR_IMAGING	11	9
<i>Rejected candidates</i>		
LIKELY_EB	9	8
FALSE_POSITIVE	3	3
GRAZING_CANDIDATE	1	1
<b>Total</b>	<b>33</b>	<b>23<sup>b</sup></b>

**Notes.** <sup>a</sup>Unique TICs per category. <sup>b</sup>Total unique TICs with signals; column does not sum due to multi-category TICs (e.g., TIC-24293836 has both PC and HR candidates, plus one LIKELY\_EB).

## 7.3. Signal Reliability Results

Individual transit events for the 20 signals have per-epoch SNR < 1; the signal emerges only after phase-folding 3–6 transits. At SDE = 7, the white-noise false alarm probability is ~1% per TLS test (Hippke & Heller 2019); correlated stellar variability increases the effective FAP, which cannot be estimated analytically for BY Dra lightcurves. The three empirical tests described in Sect. 3.5 were applied to all candidate hosts.

### 7.3.1. Circular shift FAR

A per-sector circular shift scramble test was performed on all 121 targets (Jenkins et al. 2002): each continuous sector—identified by time gaps > 5 d—receives an independent circular shift (10–90% of its length), preserving intra-sector autocorrelation while destroying inter-sector transit phase coherence. The full pipeline (TLS detection + 18-check vetting cascade) was then applied to the 121 scrambled lightcurves under identical conditions.

Of the 121 scrambled lightcurves, 21 (17.4%; Wilson 95% CI: [11.6%, 25.1%]) produced at least one candidate that passed the full search cascade (SDE ≥ 7 plus quality checks), yielding 28 individual false candidates. The false-alarm hosts span the full range of sample variability (MAD = 1 600–9 600 ppm), and their false-alarm rate (~16%) does not differ significantly from the base rate when stratified by photometric scatter, indicating

that after GP detrending the residual noise level is sufficient to generate spurious SDE ≥ 7 detections regardless of raw stellar activity. The false-alarm SDE distribution clusters near the detection threshold: median = 8.9, interquartile range 7.8–9.8, maximum = 14.1. This maximum underscores that SDE alone cannot distinguish real from spurious signals on M-dwarfs with sparse multi-sector coverage (see also Pont et al. 2006).

### 7.3.2. Lightcurve inversion test

A lightcurve inversion procedure (Coughlin et al. 2016) was applied to the 16 candidate host TICs: reflecting the flux around the baseline ( $f_{\text{inv}} = 2 - f$ ) converts all real transit dips into bumps while preserving noise variance, so that any SDE ≥ 7 detection in the inverted data establishes a per-star noise floor. Of the 16 TICs tested, 7 (44%) have SDE<sub>inv</sub> < 7 (noise floor below detection threshold), 5 (31%) have SDE<sub>inv</sub> comparable to SDE<sub>real</sub> (0.8–1.0×), and 4 (25%) are noise-dominated (SDE<sub>inv</sub> ≥ SDE<sub>real</sub>). No candidate has SDE significantly exceeding its noise floor (REAL\_EXCEEDS\_NOISE = 0). All 20 detections sit at or below their host star’s noise floor, a direct consequence of searching for small planets (100–2 000 ppm depth) on active M3–M6 dwarfs (median scatter 4 800 ppm).

### 7.3.3. Fourier per-star FAP

To quantify per-candidate significance, Fourier phase scrambling (Timmer & König 1995) was applied to all 16 candidate host TICs: per-sector FFT with randomized phases destroys all waveform coherence while preserving the power spectrum. For each TIC,  $N = 20$  scrambles were processed through the full pipeline (resolution ΔFAP = 5%); the false alarm probability (FAP) is the fraction of scrambles producing SDE ≥ SDE<sub>real</sub>.

Of the 16 TICs, 8 (50%) show FAP = 0% (0/20 exceedances; 95% CI < 16.8% by the rule of three), 2 are marginal (FAP = 10–20%), and 6 are noise-limited (FAP ≥ 25%). The two highest-MAD hosts ( $\sigma_{\text{MAD}} > 7 500$  ppm) have the worst FAP (≥ 45%), consistent with elevated stellar noise driving both real and spurious SDE peaks. Notably, 3 candidates dual-flagged by FAR and inversion nonetheless achieve FAP = 0%, indicating that their waveform morphology is not reproducible by noise alone even though the host star’s noise floor reaches comparable SDE; these candidates warrant priority monitoring for signal persistence. Per-TIC FAP values are reported in Table 11. FAP ≥ 25% downgrades one tier (Sect. 3.5).

### 7.3.4. Combined tier classification

Crossing the FAR results (per-TIC flag) with the inversion results (per-TIC noise floor) yields an initial tier assignment: 6 candidates clean on both tests, 8 single-flagged, and 6 dual-flagged. Fourier FAP refinement (Sect. 3.5) then modifies four systems: TIC 117955697 (FAP = 25%, Tier 1→2), TIC 77634567 (FAP = 45%, Tier 1→2), TIC 186664624 (FAP = 40%, Tier 2→3), and TIC 24293836 (FAP = 25%, Tier 2→3). TIC 72750190 is excluded from the tier system as a monotransit candidate (single transit epoch, MCMC unconverged; Osborn et al. 2016; Cooke et al. 2021).

The final classification of the 19 tier-assessed candidates is **2 Tier 1** (High Robustness), **7 Tier 2** (Moderate Robustness), and **10 Tier 3** (Noise-Susceptible), with 1 additional monotransit candidate (Table 11). Phase-folded lightcurves for the two Tier 1 candidates and selected Tier 2 candidates are shown in Fig. 4.

The “PLANET\_CANDIDATE” designation reflects this statistical context: these are transit-like signals warranting follow-up, not confirmed planets. The 2 Tier 1 candidates (both from TIC 211401412) are the highest-priority targets for RV confirmation. The 7 Tier 2 candidates require additional photometric confirmation (continued TESS monitoring) or RV pre-screening before resource-intensive follow-up. The 10 Tier 3 candidates cannot be distinguished from stellar noise at the current photometric sensitivity; additional TESS sectors are needed to establish signal persistence before any follow-up investment is justified.

**Table 11.** Combined signal reliability and physical verification classification for all 20 signals. The 19 tier-assessed signals are classified by FAR  $\times$  inversion  $\times$  Fourier FAP; TIC 72750190 is reported separately as a monotransit candidate.

TIC	P#	$R_p$	FAR	Inv.	FAP	Tier	Status
<i>Tier 1 — High Robustness (2)</i>							
211401412	1	1.56	Clean	BELOW	0%	1	HR
211401412	2	1.69	Clean	BELOW	0%	1	HR
<i>Tier 2 — Moderate Robustness (7)</i>							
417927999	1	0.76	FAR	BELOW	0%	2	PC
117955697	1	2.78	Clean	BELOW	25%	2 <sup>†</sup>	PC
117955697	2	3.12	Clean	BELOW	25%	2 <sup>†</sup>	PC
77634567	1	0.99	Clean	BELOW	45%	2 <sup>†</sup>	PC
266523603	1	0.68	Clean	COMP	0%	2	HR
124936003	1	0.69	Clean	COMP	0%	2	HR
322053216	1	0.96	FAR	BELOW	20%	2	HR
<i>Tier 3 — Noise-Susceptible (10)</i>							
24293836	2	1.16	Clean	DOM	25%	3 <sup>†</sup>	PC
129766762	1	0.84	FAR	DOM	30%	3	PC
139471702	1	1.57	FAR	DOM	10%	3	PC
80315364	1	0.79	FAR	DOM	95%	3	PC
24293836	1	1.72	Clean	DOM	25%	3 <sup>†</sup>	HR
419939149	1	1.01	FAR	COMP	0%	3	HR
123368775	1	0.71	FAR	COMP	0%	3	HR
65516102	1	1.00	FAR	COMP	0%	3	HR
186664624	2	2.31	FAR	BELOW	40%	3 <sup>†</sup>	HR
186664624	1	1.43	FAR	BELOW	40%	3 <sup>†</sup>	HR
<i>Monotransit (1)</i>							
72750190	1	2.01	Clean	BELOW	0%	M <sup>a</sup>	PC

**Notes.**  $R_p$  in  $R_\oplus$ . FAR: Clean = no false alarm on scrambled lightcurve; FAR =  $\geq 1$  false alarm detected. Inv.: BELOW =  $SDE_{inv} < 7$ ; COMP =  $0.8 \leq SDE_{inv}/SDE_{real} < 1$ ; DOM =  $SDE_{inv} \geq SDE_{real}$ . FAP: Fourier per-star false alarm probability ( $N = 20$  scrambles). <sup>†</sup>Tier modified by FAP refinement (FAP  $\geq 25\%$  downgrades one tier). Status: PC = PLANET\_CANDIDATE (BEB excluded); HR = NEEDS\_HR\_IMAGING (Gaia contaminants present). <sup>a</sup>Single transit epoch, MCMC unconverged; excluded from tier system (monotransit treatment per Osborn et al. 2016; Cooke et al. 2021).

## 8. Discussion

The detection of 20 transit-like signals—of which 2 achieve high robustness (Tier 1), 7 moderate robustness (Tier 2), 10 are noise-susceptible (Tier 3), and 1 is an unclassified monotransit—from a targeted 121-star survey at the stellar noise frontier warrants examination in the context of theoretical expectations, detection limitations, and the prospects for confirmation.

### 8.1. Survey Strategy in Context

The “newly enabled” selection strategy ( $\leq 2$  archival +  $\geq 1$  recent sector) deliberately targets a population overlooked by existing surveys: stars where multi-sector transit detection became possible only with TESS Cycle 6+. This complements

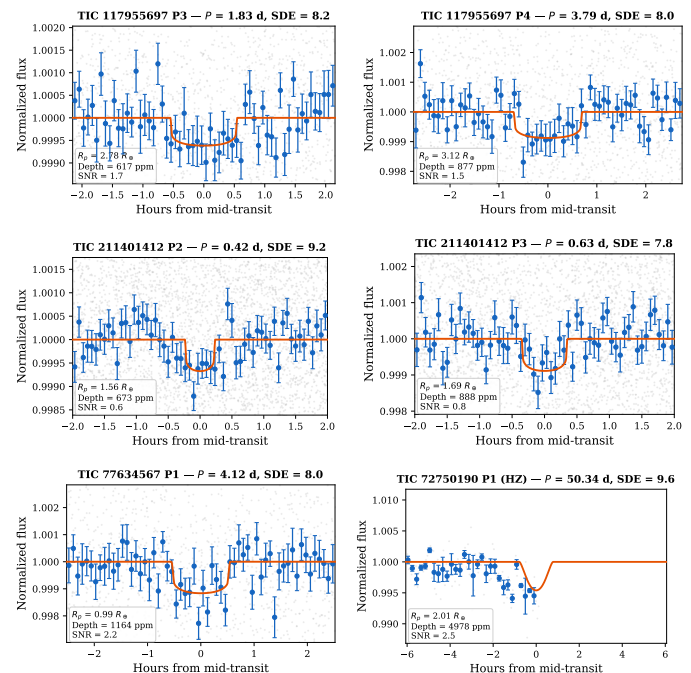


**Fig. 4.** Phase-folded lightcurves for the two Tier 1 candidates (TIC 211401412), two Tier 2 candidates downgraded by Fourier FAP (TIC 117955697, TIC 77634567), and the monotransit candidate TIC 72750190. **Top row:** TIC 117955697 P1 ( $P = 1.83$  d, Tier 2) and P2 ( $P = 3.79$  d, Tier 2). **Middle row:** TIC 211401412 P1 ( $P = 0.42$  d, Tier 1) and P2 ( $P = 0.63$  d, Tier 1). **Bottom row:** TIC 77634567 ( $P = 4.12$  d, Tier 2) and TIC 72750190 ( $P = 50.3$  d, monotransit, tentative HZ). Grey points: individual TLS phase-folded measurements. Blue circles with error bars: mean-binned data (60 bins, SEM). Orange curve: batman transit model (Kreidberg 2015) with quadratic limb darkening (TESS bandpass; Claret 2017); shape parameters from MCMC posterior medians, depth scaled to match the TLS-observed transit depth. TIC 72750190 uses a TLS box-model estimate (MCMC did not converge; single transit).

rather than competes with SPOC/QLP real-time processing (limited to  $P < 13$  d), QLP multi-sector searches ( $T_{mag} < 10.5$ ), and archival continuous viewing zone (CVZ) surveys focusing on well-observed targets ( $> 13$  sectors). The survey’s primary strength is its sensitivity to small planets around the smallest stars: the M3–M6 restriction ensures transit depths  $> 800$  ppm for Earth-sized planets, enabling the sub-Earth detections that constitute the most distinctive aspect of the catalog.

A consequence of the “newly enabled” selection is that temporal coverage is inherently sparse: typically 3–10 sectors (median 4) spread across 2–4 TESS cycles, producing heavily gapped baselines (700–2 600 d of baseline with only  $\sim 80$ –160 d of photometry). This creates severe window-function artifacts, particularly at long periods where  $\leq 3$  transit events are observed. The 3-sector limit test confirms that 0/5 planets with  $P > 10$  d are recovered at the survey minimum, and harmonic aliasing is exacerbated (e.g., L 98-59 c detected at  $P/2$ ). The 18-check signal validation cascade (Sect. 3.3) and the evidence-based harmonic breaker (Sect. 3.2.1) mitigate these effects, but cannot entirely eliminate them. The 81% non-detection rate (98/121) is expected given the combination of sparse temporal sampling and BY Dra stellar variability on active M-dwarfs.

## 8.2. Methodology Transferability and Testable Predictions

The three contributions of this work—the 18-check signal validation cascade, the three-test reliability framework (FAR, inversion, Fourier FAP), and the tier classification system—address a general problem in time-domain astrophysics: classifying transit-like signals when correlated stellar noise produces false alarms at rates comparable to genuine detections. This problem extends well beyond the M3–M6 sample studied here.

**K5–M2 dwarfs.** For earlier M-dwarfs and late K-dwarfs ( $R_\star \approx 0.4\text{--}0.6 R_\odot$ ), Earth-sized transits produce depths of 300–800 ppm—below the noise floor of most TESS targets with  $\leq 5$  sectors. Thousands of K5–M2 dwarfs are currently transitioning from single-sector to multi-sector TESS coverage as the extended mission accumulates observations, creating a “newly enabled” population analogous to the M3–M6 sample of this work but with shallower transits and correspondingly more severe noise contamination. The tier system and FAR/inversion framework are directly applicable: the circular shift test preserves the host star’s autocorrelation structure regardless of spectral type, and the inversion test establishes a per-star noise floor that scales naturally with variability amplitude. The key modification is the expected tier distribution: a higher fraction of Tier 3 (Noise-Susceptible) candidates is predicted on K5–M2 hosts due to the smaller  $(R_p/R_\star)^2$  transit depth ratio.

**Young and pre-main-sequence stars.** M-dwarfs younger than  $\sim 1$  Gyr exhibit photometric variability 5–50 $\times$  larger than field stars of the same spectral type, driven by starspot evolution, magnetic activity cycles, and heightened flare rates (Newton et al. 2017). K2 campaigns on young open clusters (Hyades, Praesepe, Upper Scorpius; Mann et al. 2017) and ongoing TESS monitoring of young moving group members have produced candidate transit detections on extremely active hosts. For these targets, the noise frontier problem is even more severe than for the field M3–M6 dwarfs in this survey: BY Dra modulation amplitudes of 2–5% routinely exceed transit depths by an order of magnitude, even after GP detrending. The FAR and inversion tests are particularly valuable in this regime because they quantify the host star’s capacity to produce false SDE  $\geq 7$  detections from variability alone, providing a per-star noise calibration that purely analytical false alarm probabilities cannot capture on non-Gaussian lightcurves.

**Ultracool dwarfs (M7–L).** Ground-based transit surveys targeting the latest M-dwarfs and L-dwarfs (SPECULOOS, TRAPPIST; Sebastian et al. 2021; Gillon et al. 2017) face a compounded noise floor: atmospheric scintillation and telluric absorption add red noise components absent from space-based photometry, while the intrinsic stellar variability of ultracool dwarfs remains significant. Transit depths are deep ( $>1\%$  for Earth-sized planets around  $R_\star < 0.12 R_\odot$ ), but the detection challenge shifts from signal amplitude to systematic noise discrimination. The tier framework—particularly the Fourier phase scrambling test, which preserves the power spectrum while destroying waveform coherence—provides a noise model that is agnostic to the physical origin of the red noise (stellar, atmospheric, or instrumental).

**PLATO long-duration monitoring.** The PLATO mission (Rauer et al. 2024) will observe  $\sim 245\,000$  FGK stars continuously for 2+ years with  $\sim 25$ -second cadence. While its primary targets are bright ( $V < 11$ ), the faint end of the PLATO sample will operate near the photon-noise detection limit, where correlated instrumental systematics can produce false transit-like signals analogous to the stellar noise floor characterized here. The tier system’s three-test approach—circular shift

FAR for population-level false alarm rates, lightcurve inversion for per-star noise floors, and Fourier FAP for per-candidate significance—provides a classification layer complementary to PLATO’s own detection and vetting pipelines.

**Testable prediction: the TESS continuous viewing zone.** The principal limitation of this survey—sparse temporal coverage (median 4 sectors,  $\sim 80$  d of photometry)—produces a concrete, testable prediction. The TESS CVZ provides M3–M6 dwarfs with 30–44 sectors accumulated over 6 years of observations. The  $\sqrt{N}$  scaling of SDE with transit count predicts a  $\sim 3.4\times$  gain, sufficient to lift genuine signals above the noise floor. Three outcomes are predicted: (1) some Tier 1–2 signals persist and strengthen with additional sectors, confirming planetary origin; (2) all signals remain at the noise floor despite 10 $\times$  more data, establishing a stellar variability ceiling for TLS detection on M-dwarfs; or (3) new signals emerge that were undetectable with sparse coverage, constraining the occurrence rate of small planets around active M-dwarfs. Each outcome directly extends the noise frontier characterization established here and informs the optimal resource allocation for follow-up campaigns.

## 9. Conclusions

This survey of 121 “newly enabled” M3–M6 dwarfs identified 20 transit-like signals across 16 systems—none with prior TOI designations—and mapped the detection parameter space of TLS on active M-dwarfs with sparse multi-sector coverage.

1. **A validated pipeline:** 100% recovery on 16 known planets with 0 false positives. The three-test signal reliability framework (circular shift FAR, lightcurve inversion, Fourier phase scrambling) provides a transparent classification system applicable to any noise-dominated detection regime.
2. **Where planets are detectable:** Injection tests identify the parameter space where the pipeline successfully recovers planets despite stellar noise: short periods ( $P < 5$  d, recovery 73% on calm hosts), large radii ( $R_p \geq 2 R_\oplus$ , recovery 85%), and late M-dwarfs (M5–M6) where the  $(R_p/R_\star)^2$  depth advantage compensates for elevated variability. Two Tier 1 candidates on TIC 211401412 (FAP = 0%, clean FAR, SDE below noise floor) are the highest-priority targets for RV confirmation.
3. **The noise frontier:** No candidate SDE exceeds its host star’s noise floor (REAL\_EXCEEDS\_NOISE = 0); the global FAR is 17.4% (Wilson 95% CI: [11.6%, 25.1%]). With 3–10 sectors, stellar variability on M3–M6 dwarfs produces false detections at rates indistinguishable from transit signals (SDE  $\sim 7\text{--}12$ ), confirming a 3.1 $\times$  recovery degradation from calm to active hosts (Yaptangco et al. 2025).
4. **Pathways to discovery:** The TESS continuous viewing zone (30–44 sectors,  $\sim 3.4\times$  SDE gain) can resolve the classification ambiguity for the signals identified here. Beyond TESS, the tier framework and validation cascade are directly transferable to K5–M2 dwarfs entering multi-sector coverage, young stellar populations where variability amplitudes are 5–50 $\times$  larger ( $<1$  Gyr; K2 clusters, TESS young groups), ultracool dwarfs targeted by ground-based surveys (SPECULOOS; Sebastian et al. 2021), and the faint end of the PLATO sample (Rauer et al. 2024). In each case, the pipeline maps the boundary between detectable and noise-dominated parameter space, enabling targeted allocation of follow-up resources.

## Data availability

Full candidate tables are available in electronic form at the CDS via anonymous ftp to [cdsarc.u-strasbg.fr](ftp://cdsarc.u-strasbg.fr) (130.79.128.5) or via <https://cdsarc.cds.unistra.fr>. Pipeline code and candidate data are available at <https://gitlab.com/yohannschudi/exoplanets-project>. TESS photometry was obtained from the Mikulski Archive for Space Telescopes (MAST) at STScI (<https://mast.stsci.edu>).

*Acknowledgements.* This work used TESS data from the Mikulski Archive for Space Telescopes (MAST) at STScI. Analysis was performed using Python 3.11 with `lightkurve` 2.4, `transitleastquares` 1.0.31, `triceratops` 1.0.18, `celerite2` 0.3, `emcee` 3.1, and `batman` 2.4. The author thanks the development teams of these packages. Transit searches ran on Apple M-series and Intel Xeon CPUs (~800 CPU-hours total). *AI transparency:* Pipeline code was developed with assistance from Claude (Anthropic) for code generation and debugging, with cross-validation by Gemini (Google) for algorithm design review. All AI-generated code was reviewed, tested, and validated by the author. The manuscript text was written by the author; AI tools were used for language editing only. The full development history is preserved in the version control repository.

## References

- Barkaoui, K. et al. 2024, A&A, 687, A261  
 Batalha, N. M. et al. 2013, ApJS, 204, 24  
 Bryson, S. T. et al. 2013, PASP, 125, 889  
 Chambers, J. E., Wetherill, G. W., & Boss, A. P. 1996, Icarus, 119, 261  
 Claret, A. 2017, A&A, 600, A30  
 Cooke, B. F., Pollacco, D., Lendl, M., et al. 2021, MNRAS, 500, 5088  
 Coughlin, J. L. et al. 2016, ApJS, 224, 12  
 Crossfield, I. J. M., Waalkes, W., Newton, E. R., et al. 2019, ApJ, 883, L16  
 Delrez, L. et al. 2022, A&A, 667, A59  
 Dévora-Pajares, M., Pozuelos, F. J., et al. 2024, MNRAS, 532, 4752  
 Dholakia, S. et al. 2024, MNRAS, 531, 1276  
 Dressing, C. D. & Charbonneau, D. 2015, ApJ, 807, 45  
 Fabricius, C. et al. 2021, A&A, 649, A5  
 Fabrycky, D. C. et al. 2014, ApJ, 790, 146  
 Fausnaugh, M. M. et al. 2018, TESS Data Release Notes: Sectors 1–69, Tech. Rep. NASA/TM-2018-220190, NASA Goddard Space Flight Center, updated per sector; documents 1-day Earth rotation systematic  
 Foreman-Mackey, D. et al. 2013, PASP, 125, 306  
 Foreman-Mackey, D. et al. 2017, AJ, 154, 220  
 Gaia Collaboration. 2023, A&A, 674, A1  
 Giacalone, S. & Dressing, C. D. 2020, AJ, 159, 169  
 Giacalone, S. et al. 2021, AJ, 161, 24  
 Gilbert, E. A. et al. 2020, AJ, 160, 116  
 Gillon, M., Triaud, A. H. M. J., Demory, B.-O., et al. 2017, Nature, 542, 456  
 Gladman, B. 1993, Icarus, 106, 247  
 Guerrero, N. M. et al. 2021, ApJS, 254, 39  
 Henry, T. J. et al. 2006, AJ, 132, 2360  
 Hippke, M. & Heller, R. 2019, A&A, 623, A39  
 Hippke, M. et al. 2019, AJ, 158, 143  
 Jenkins, J. M., Caldwell, D. A., & Borucki, W. J. 2002, ApJ, 564, 495  
 Kemmer, J. et al. 2020, A&A, 642, A236  
 Kempton, E. M.-R. et al. 2018, PASP, 130, 114401  
 Kostov, V. B. et al. 2019, AJ, 158, 32  
 Kreidberg, L. 2015, PASP, 127, 1161  
 Kunimoto, M., Shallue, C. J., Vanderburg, A., & Gill, S. 2025, AJ, 169, 42  
 Lightkurve Collaboration. 2018, Lightkurve: Kepler and TESS time series analysis in Python, Astrophysics Source Code Library, record ascl:1812.013  
 Lindgren, L. et al. 2021, A&A, 649, A2  
 Luque, R. et al. 2019, A&A, 628, A39  
 Mann, A. W., Gaidos, E., Vanderburg, A., et al. 2017, AJ, 155, 4  
 Mann, A. W. et al. 2015, ApJ, 804, 64  
 Ment, K. & Charbonneau, D. 2023, AJ, 165, 265  
 Newton, E. R., Irwin, J., Charbonneau, D., et al. 2017, ApJ, 834, 85  
 Osborn, H. P., Armstrong, D. J., Brown, D. J. A., et al. 2016, MNRAS, 457, 2273  
 Peterson, M. S., Benneke, B., Collins, K., et al. 2023, Nature, 617, 701  
 Plavchan, P. et al. 2020, Nature, 582, 497  
 Pont, F., Zucker, S., & Queloz, D. 2006, MNRAS, 373, 231  
 Rao, S., Mahabal, A., Rao, N., & Raghavendra, C. 2021, MNRAS, 502, 2845  
 Rauer, H., Catala, C., Aerts, C., et al. 2024, Experimental Astronomy, 58, 2  
 Ricker, G. R. et al. 2015, JATIS, 1, 014003  
 Santerne, A. et al. 2013, A&A, 557, A139  
 Sebastian, D., Gillon, M., Ducrot, E., et al. 2021, A&A, 645, A100  
 Stassun, K. G. et al. 2019, AJ, 158, 138  
 Sullivan, P. W. et al. 2015, ApJ, 809, 77  
 Thompson, S. E. et al. 2018, ApJS, 235, 38  
 Timmer, J. & König, M. 1995, A&A, 300, 707  
 Trifonov, T. et al. 2021, Science, 371, 1038  
 Twicken, J. D. et al. 2018, PASP, 130, 064502  
 Yaptangco, G., Ballard, S., & Dittmann, J. 2025, AJ, 169, 153  
 Zechmeister, M. & Kürster, M. 2009, A&A, 496, 577

## Appendix A: Complete Candidate Catalog

**Table A.1.** Complete survey statistics.

Metric	Value	Notes
Stars analyzed	121	Complete sample
No detection	98	81.0%
With signals	23	19.0%
Post-cleanup	33	Harmonic nest cleanup v1.1
Surviving	20	16 systems
Multi-planet	8 cand.	4 systems
TOI crossmatch	0	—
PLANET_CAND	9 / 8 sys	BEB excluded or LIKELY_PLANET
NEEDS_HR	11 / 9 sys	HR imaging required
LIKELY_EB	9 / 8 sys	Eclipsing binary
FALSE_POS	3 / 3 sys	Contamination certain
GRAZING	1 / 1 sys	Radius uncertain

**Notes.** Excludes 13 harmonic nests and LIKELY\_EB/FALSE\_POSITIVE signals from post-cleanup count.

### A.1. PLANET\_CANDIDATE

**Table A.2.** PLANET\_CANDIDATE: Exhaustive parameters. Ordered by signal reliability tier (Sect. 3.5); monotransit last.

TIC	P#	P (d)	$T_0$ (BTJD)	Depth (ppm)	SDE	$R_p$ ( $R_\oplus$ )	$T_{\text{eq}}$ (K)	S ( $S_\oplus$ )	$T_{\text{mag}}$	d (pc)	RUWE	Tier	HZ
117955697	1	1.833	2854.62	617	8.20	$2.78^{+0.06}_{-0.08}$	$605 \pm 55$	31.74	11.82	32.6	1.30	2	
117955697	2	3.789	2855.08	877	7.96	$3.12^{+0.08}_{-0.07}$	$475 \pm 43$	12.05	11.82	32.6	1.30	2	
77634567	1	4.123	1792.04	1164	8.04	$0.99^{+0.14}_{-0.14}$	$415 \pm 38$	7.03	12.36	30.7	1.33	2	
417927999	1	1.574	1817.19	737	9.20	$0.76^{+0.17}_{-0.16}$	$609 \pm 55$	32.66	11.75	26.4	1.24	2	
24293836	2	16.242	1328.05	1316	8.55	$1.16^{+0.25}_{-0.24}$	$284 \pm 26$	1.54	11.51	26.1	$1.30^\dagger$	$3^\ddagger$	
129766762	1	1.122	1386.15	626	8.03	$0.84^{+0.08}_{-0.09}$	$681 \pm 62$	51.01	12.22	33.6	$1.31^\dagger$	3	
139471702	1	41.184	1398.45	2526	8.72	$1.57^{+0.32}_{-0.31}$	$205 \pm 19$	0.42	12.39	37.3	1.21	3	Yes
80315364	1	22.122	2095.39	2173	7.84	$0.79^{+0.17}_{-0.16}$	$186 \pm 17$	0.28	12.37	14.6	1.37	3	Yes
72750190	1	50.340	1407.16	4978	9.60	$2.01^*$	$187 \pm 17$	0.29	12.14	31.1	$1.15^\ddagger$	M <sup>§</sup>	Tent. <sup>‡</sup>

**Notes.**  $R_p$  from MCMC unless noted.  $T_{\text{eq}}$  assumes Bond albedo  $A = 0.3$ ; uncertainties propagated from TIC v8.2 stellar radii ( $\sigma_{R_\star}/R_\star \approx 3\%$ , combined with  $T_{\text{eff}}$  uncertainties, yielding  $\sim 9\%$  on  $T_{\text{eq}}$ ). Tier = signal reliability tier (Sect. 3.5): 1 = High Robustness, 2 = Moderate Robustness, 3 = Noise-Susceptible; M = monotransit (excluded from tier system). <sup>†</sup>LIKELY\_PLANET protected: Gaia contaminant(s) present or Gaia coverage incomplete, but TRICERATOPS FPP < 50%; HR imaging recommended. <sup>\*</sup>TLS box-model estimate (MCMC did not converge). <sup>‡</sup>Tentative HZ detection: single transit epoch, MCMC failed; excluded from HZ candidate count. <sup>§</sup>Monotransit candidate: single transit epoch, excluded from tier system per Osborn et al. (2016); Cooke et al. (2021).

#### A.1.1. Host Star Parameters

**Table A.3.** Host star parameters for PLANET\_CANDIDATE systems.

TIC	SpT	$T_{\text{eff}}$ (K)	$R_\star$ ( $R_\odot$ )	$M_\star$ ( $M_\odot$ )	$T_{\text{mag}}$	d (pc)	Cand.
80315364	M5V	2953	0.16	0.13	12.37	14.6	1
77634567	M3V	3211	0.27	0.24	12.36	30.7	1
72750190	M3V	3259	0.29	0.27	12.14	31.1	1
129766762	M3V	3323	0.30	0.27	12.22	33.6	1
139471702	M3V	3347	0.29	0.26	12.39	37.3	1
24293836	M3V	3369	0.30	0.27	11.51	26.1	1 <sup>a</sup>
417927999	M3V	3374	0.28	0.26	11.75	26.4	1
117955697	M3V	3376	0.33	0.31	11.82	32.6	2

**Notes.** Cand. = number of candidates per system. <sup>a</sup>+1 NEEDS\_HR\_IMAGING (P1).

## A.2. NEEDS\_HR\_IMAGING

**Table A.4.** NEEDS\_HR\_IMAGING: Exhaustive parameters. Contam. = number of Gaia sources with  $G < G_{\max}$  within 30".

TIC	P#	P (d)	Depth (ppm)	SDE	$R_p$ ( $R_{\oplus}$ )	$T_{\text{eq}}$ (K)	S ( $S_{\oplus}$ )	FPP (%)	Contam.	Margin	HZ
186664624	2	47.594	3995	8.07	$2.31^{+0.47}_{-0.48}$	$204 \pm 19$	0.41	60	2	+0.4	Yes
186664624	1	82.218	1497	8.38	$1.43^{+0.28}_{-0.29}$	$170 \pm 15$	0.20	77	3	+1.5	No
24293836	1	17.674	1145	8.25	$1.72^{+0.13}_{-0.13}$	$276 \pm 25$	1.37	53	2	+1.2	No
65516102	1	9.198	1236	9.45	$1.00^{+0.19}_{-0.19}$	$324 \pm 29$	2.62	66	1	+1.4	No
322053216	1	6.560	830	8.60	$0.96^{+0.21}_{-0.15}$	$376 \pm 34$	4.74	61	1	+1.3	No
124936003	1	1.156	952	10.71	$0.69^{+0.16}_{-0.12}$	$602 \pm 55$	31.21	67	2	+3.8	No
266523603	1	1.034	471	9.88	$0.68^{+0.11}_{-0.12}$	$732 \pm 67$	68.23	62	1	+0.4	No
123368775	1	0.727	358	9.79	$0.71^{+0.10}_{-0.11}$	$812 \pm 74$	103.20	58	1	+1.6	No
419939149	1	0.547	987	9.16	$1.01^{+0.09}_{-0.29}$	$901 \pm 82$	156.22	53	0*	—	No
211401412	1	0.422	673	9.18	$1.56^{+0.04}_{-0.03}$	$931 \pm 85$	177.80	58	3*	+3.2	No
211401412	2	0.629	888	7.81	$1.69^{+0.05}_{-0.03}$	$815 \pm 74$	104.38	57	3*	+2.9	No

**Notes.**  $R_p$  in  $R_{\oplus}$  from MCMC.  $T_{\text{eq}}$  uncertainties as in Table A.2. Margin = brightest contaminant magnitude minus  $G_{\max}$ . \*Gaia incomplete at required  $G_{\max}$ .

## A.2.1. Imaging Requirements

**Table A.5.** HR imaging requirements and recommended facilities.

TIC	$G_{\max}$	Marg.	Diff.	Facility
186664624	18.5–19.5	+0.4	Tight	Gemini/Alopeke
24293836	18.9	+1.2	Med.	SOAR/HRCam
65516102	19.7	+1.4	Easy	Any speckle
322053216	19.2	+1.3	Easy	Any speckle
124936003	19.8	+3.8	Easy	Any speckle
266523603	19.7	+0.4	Tight	Gemini/Alopeke
123368775	20.3*	+1.6	Med.	SOAR/HRCam
419939149	20.0*	N/A	Hard	Keck/NIRC2
211401412	20.1–20.4*	+2.9	Easy	Any speckle

**Notes.** Marg. = brightest contaminant  $G - G_{\max}$ . \*Gaia incomplete; deep AO required.

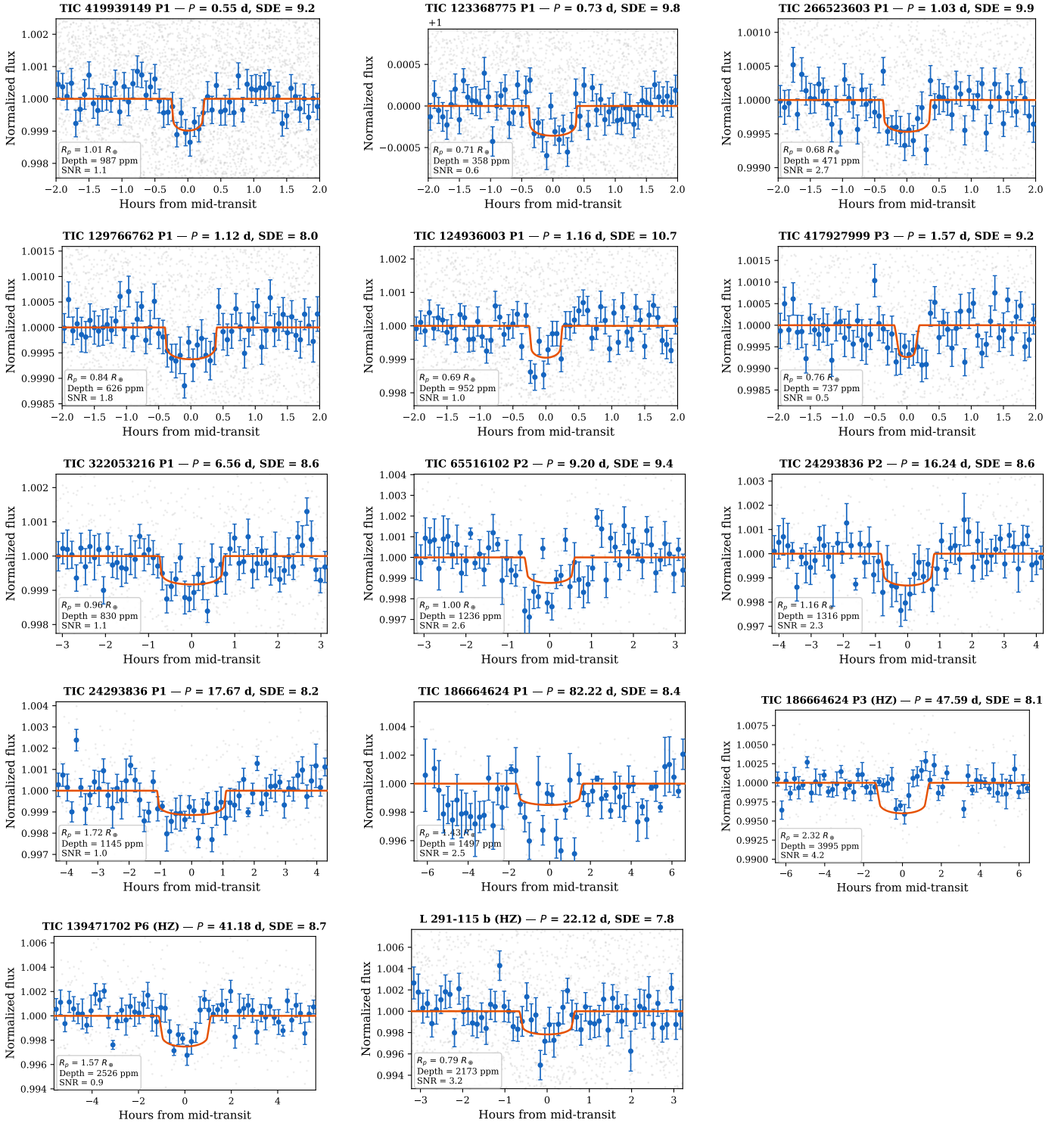


**Fig. A.1.** Phase-folded lightcurves for the 14 candidates not shown in Fig. 4 (PLANET\_CANDIDATE and NEEDS\_HR\_IMAGING), ordered by orbital period. Format as in Fig. 4. Grey: individual measurements; blue: mean-binned data; orange: batman model with MCMC shape parameters. The three HZ candidates (TIC 186664624 P2, TIC 139471702, TIC-80315364; all Tier 3) are included here. TIC 72750190 ( $P = 50.3$  d, tentative HZ, monotransit) is excluded: MCMC did not converge due to a single partial transit.

## A.3. GRAZING\_CANDIDATE

**Table A.6.** GRAZING\_CANDIDATE parameters.

TIC	P (d)	SDE	$R_p^*$	$b$	$T_{\text{eq}}$
65516102	0.97	11.13	0.72	1.07	728

**Notes.** \*Radius ( $R_p$ ) highly uncertain; grazing geometry ( $b > 1$ ).

## A.4. LIKELY\_EB

**Table A.7.** LIKELY\_EB candidates and rejection reasons.

TIC	P (d)	SDE	FPP	Reason
206596030	97.27	10.2	28	Dur. anomaly
206596030	50.31	11.4	45	prob_eb 25%
85595350	80.30	8.7	60	Dur. anomaly
53845811	67.56	12.6	56	MCMC fail + EB
139471702	70.94	9.6	95	NFPP = 91%
36727984	53.74	11.2	70	Dur. anomaly
417927999	38.13	9.6	58	prob_eb 33%
117955697	9.55	8.3	64	2nd eclipse
24293836	4.90	8.6	53	2nd eclipse

**Notes.** FPP in %. Rejected signals are identified by orbital period; they do not carry planet numbers.

## A.5. FALSE\_POSITIVE

**Table A.8.** FALSE\_POSITIVE systems and rejection reasons.

TIC	P (d)	FPP	Reason
24292625	47.13	100%	NFPP = 100%
123849672	75.92	100%	NFPP = 100%
436558874	39.93	62%	prob_eb 39%

## Appendix B: Target Sample

**Table B.1.** M3–M6 sample summary statistics.

Parameter	Range	Median
$T_{\text{eff}}$ (K)	2848–3397	3280
$T_{\text{mag}}$	8.34–12.50	11.97
$R_*$ ( $R_{\odot}$ )	0.147–0.349	0.280
$M_*$ ( $M_{\odot}$ )	0.120–0.333	0.256
RUWE	1.00–1.39	1.05
Distance (pc)	5.2–48.2	26.5
N sectors	3–10	4
Baseline (d)	735–2602	1847

**Table B.2.** Sample distribution by spectral type and detection outcome.

Type	$T_{\text{eff}}$ (K)	N	Signals	Det. rate
M6	<2900	2	0	0%
M4–M5	2900–3200	22	6	27.3%
M3	3200–3400	97	17	17.5%
<b>Total</b>	2848–3397	<b>121</b>	<b>23</b>	<b>19.0%</b>

## Appendix C: Validation Results

**Table C.1.** Complete validation sample: 10 systems meeting criteria, 16 TESS-detectable planets, 100% recovery. LHS 1140 tested separately as limit case.

System	TIC	SpT	d (pc)	$T_{\text{mag}}$	Planets	HZ	Gaia	Status
L 98-59	307210830	M3V	10.6	9.39	3	—	0	PLANET_CAND
TOI-700	150428135	M2V	31.1	10.95	4	d	2–5	NEEDS_HR
Gliese 12	52005579	M4V	12.2	10.18	1	b	0	PLANET_CAND
GJ 357	413248763	M2.5V	9.4	8.74	1	—	2	NEEDS_HR
GJ 3473	452866790	M4V	27.4	11.20	1	—	0	PLANET_CAND
GJ 486	390651552	M3.5V	8.1	8.07	1	—	0	PLANET_CAND
TOI-406	153065527	M4V	22.0	11.28	1	—	1	NEEDS_HR
TOI-782	429358906	M3V	57.0	12.29	1	—	1	NEEDS_HR
TOI-6086	18318288	M3.5V	32.0	12.41	1	—	1	NEEDS_HR
LP 791-18	181804752	M5V	26.5	13.56	2 <sup>†</sup>	—	1–2	NEEDS_HR
<b>Total</b>					<b>16</b>	<b>2</b>		<b>6 PC / 10 HR</b>

**Notes.** Gaia = contaminants within 30'' brighter than  $R_{p,\text{max}}$ . <sup>†</sup>LP 791-18 d excluded (Spitzer discovery, Peterson et al. 2023).

**Table C.2.** Validation planet detection parameters and NASA Archive comparison.

System	Pl.	$P_{\text{det}}$ (d)	$P_{\text{arch}}$ (d)	$\Delta P/P^a$	SDE	Depth	$R_p$	FPP	NFPF
L 98-59	b	2.2531	2.2531	<0.01%	56.3	596	0.80	33%	26%
L 98-59	c	3.6908	3.6907	<0.01%	54.9	1656	1.38	0.6%	0.6%
L 98-59	d	7.3810	7.4507	0.94% <sup>b</sup>	65.1	1279	1.49	2.9%	2.5%
TOI-700	b	9.9769	9.9770	<0.01%	37.6	453	1.01	29%	20%
TOI-700	c	16.051	16.051	<0.01%	49.4	2079	2.63	33%	16%
TOI-700	d	37.426	37.426	<0.01%	28.2	575	1.14	25%	15%
TOI-700	e	27.811	27.809	<0.01%	18.5	388	0.95	43%	22%
Gliese 12	b	12.761	12.761	<0.01%	23.5	1047	1.00	35%	17%
GJ 357	b	3.9306	3.9306	<0.01%	48.5	1023	1.26	20%	13%
GJ 3473	b	1.1980	1.1980	<0.01%	37.9	1239	1.51	21%	17%
GJ 486	b	1.4671	1.4671	<0.01%	27.9	1705	1.31	18%	14%
TOI-406	b	13.176	13.176	<0.01%	30.4	2255	1.88	16%	7%
TOI-782	b	8.0240	8.0240	<0.01%	36.4	3549	2.48	28%	20%
TOI-6086	b	1.3889	1.3889	<0.01%	32.4	1705	0.95	61%	57%
LP 791-18	c	4.9899	4.9899	<0.01%	46.1	17086	2.13	39%	28%
LP 791-18	b	0.9480	0.9480	<0.01%	42.9	4023	1.12	61%	53%

**Notes.** Depth in ppm.  $R_p$  in  $R_{\oplus}$ . FPP/NFPF from TRICERATOPS. <sup>a</sup> $\Delta P/P = |P_{\text{det}} - P_{\text{arch}}|/P_{\text{arch}}$ . <sup>b</sup>L 98-59 d is detected at  $P = 7.381$  d rather than the archive value of 7.451 d (0.94% offset); this exceeds the 0.2% injection-recovery tolerance (Sect. 4.1) but is unambiguously the correct planet (SDE = 65.1, highest in the system). The period offset likely results from iterative masking of planets b and c prior to the search for planet d.

**Table C.3.** Gaia DR3 verification for validation planets.

System	Pl.	$G_{\max}$	Ct.	RUWE	Status
L 98-59	b	17.5	0	1.27	PC
L 98-59	c	16.4	0	1.27	PC
L 98-59	d	16.6	0	1.27	PC
TOI-700	b	19.3	5	1.03	HR
TOI-700	c	17.6	2	1.03	HR
TOI-700	d	19.0	5	1.03	HR
TOI-700	e	19.4	5	1.03	HR
Gliese 12	b	17.6	0	1.20	PC
GJ 357	b	16.2	2	1.12	HR
GJ 3473	b	18.5	0	1.30	PC
GJ 486	b	16.8	0	1.09	PC
TOI-406	b	17.9	1	1.26	HR
TOI-782	b	18.4	1	1.25	HR
TOI-6086	b	19.3	1	1.20	HR
LP 791-18	c	18.0	1	1.12	HR
LP 791-18	b	19.5	2	1.12	HR
LHS 1140 <sup>†</sup>	b	16.8	1	<b>1.53</b>	HR
LHS 1140 <sup>†</sup>	c	17.5	1	<b>1.53</b>	HR

**Notes.** Ct. = Gaia contaminants ( $G < G_{\max}, < 30''$ ). PC = PLANET\_CANDIDATE, HR = NEEDS\_HR\_IMAGING. <sup>†</sup>Limit test (2 sectors, RUWE > 1.4).